

A PHYSICS-BASED SINGLE CRYSTAL PLASTICITY MODEL FOR CRYSTAL  
ORIENTATION AND LENGTH SCALE DEPENDENCE OF MACHINING RESPONSE

by

CANSET MERCAN

Submitted to the Graduate School of Engineering and Natural Sciences  
in partial fulfillment of  
the requirements for the degree of  
Master of Engineering

Sabanci University July 2018

A PHYSICS-BASED SINGLE CRYSTAL PLASTICITY MODEL FOR CRYSTAL  
ORIENTATION AND LENGTH SCALE DEPENDENCE OF MACHINING RESPONSE

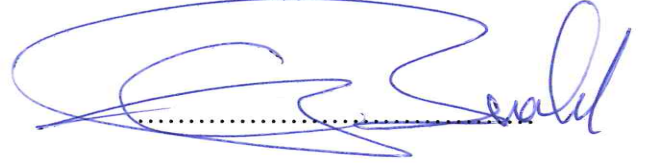
APPROVED BY:

Asst. Prof. Dr. Eralp Demir  
(Thesis Supervisor)



.....

Prof. Dr. Erhan Budak



.....

Asst. Prof. Dr. Umut Karagüzel



.....

DATE OF APPROVAL: 31.07.2018

© Canset MERCAN 2018

All Rights Reserved

To my family...

## ABSTRACT

### *A PHYSICS-BASED SINGLE CRYSTAL PLASTICITY MODEL FOR CRYSTAL ORIENTATION AND LENGTH SCALE DEPENDENCE OF MACHINING RESPONSE*

*Canset MERCAN*

*Manufacturing Engineering, MSc. Thesis, 2018*

*Supervisor: Assist. Prof. Dr. Eralp DEMIR*

*July 2018, 79 pages*

**Keywords:** single crystal machining, crystal plasticity, physics-based modeling, micro machining, workpiece anisotropy, machining size dependence

Recent demands towards the miniaturization raises the importance of micro-machining, which is one of the most flexible manufacturing process. The cutting parameters such as depth of cut, tool diameter etc. have become comparable to the dimensions of the crystals during machining at micro scale which effects on the machining response of the material. Due to the highly anisotropic behavior of single crystals, it is important to consider the effect of the crystallographic orientation on the cutting response. Size-dependency of the cutting response is defined as the non-linear increase in specific cutting energy with the reduction in the uncut chip thickness. Size dependence has to be also considered in machining models since it could affect the chip formation process, cutting forces and the stability.

In this work, micro-machining model based on crystal plasticity kinematics and physics based constitutive descriptions is developed for FCC single crystals. The proposed model contains constitutive laws that are based on physics-based material state variables. The size-effect is also

incorporated to the physics based constitutive laws as an additional strain hardening term that is a function of the amount of shear and shear plane length. Size dependence is related to the nature of the shearing process being confined to smaller shear planes as the depth of cut decreases and the corresponding increase in the statistically stored dislocation density. In this work the effect of edge radius is not considered and the effect of strain-rate is present. The total work is minimized to find the shear angle for any given crystal orientation and the selected machining parameters. The model is applied simulate the experimental force fluctuations of single crystals of aluminum and copper in Cohen's work with a reasonably good agreement.

## ÖZET

*TEK KRİSTAL MALZEMELERİN TALAŞLI İMALAT TEPKİSİNİN KRİSTAL KONUMU VE UZUNLUK ÖLÇEĞİ BAĞIMLILIĞI İÇİN FİZİKSEL TEMELLİ KRİSTAL PLASTİSİTE MODELİ*

*Canset MERCAN*

*Üretim Mühendisliği, Yüksek Lisans Tezi, 2018*

*Tez Danuşmanı: Dr. Öğretim Üyesi Eralp DEMİR*

*Temmuz 2018, 79 sayfa*

**Anahtar Kelimeler:** tek kristalli malzeme talaşlı imalat, kristal plastisite, fiziksel temelli modelleme, hassas talaşlı imalat, kristal anizotropisi, talaşlı imalatta boyut etkisi

Minyatürleşmeye yönelik son eğilimler ve talepler, esnekliği en fazla olan mikro-seviye üretim yöntemlerinden biri olan hassas talaşlı imalat prosesinin ve teknolojilerinin önemini arttırmıştır. Mikro seviye talaşlı imalat esnasında kesme derinliği, takım radyusu gibi parametreler, kristal ölçüleri ile kıyaslanabilir seviyelerde olduğu için malzemenin kristal oryantasyonunun, kesme ve plastik deformasyon esnasında malzeme tepkisi üzerinde ciddi bir etkisi olmaktadır. Tek kristal malzemelerin gösterdiği yüksek anizotropik davranış nedeniyle mikro seviyelerde yapılan bu kesme işlemleri için oluşturulacak analitik modellerde, kristal anizotropisinin; kesme kuvvetleri ve yüzey kalitesi gibi kesme tepkisi üzerine olan etkilerinin göz önünde bulundurulması gerekmektedir. Boyut (büyüklük) etkisi ise spesifik kesme enerjisinde, deforme olmamış talaş kalınlığındaki düşüğe bağlı olarak gerçekleşen ani ve lineer olmayan yükseliş olarak tanımlanmaktadır. Boyut etkisi talaş oluşum prosesini, kesme kuvvetlerini ve tezgah stabilitesini etkileyebildiği için talaşlı imalat işlemleri için oluşturulacak analitik modellerde, bu faktörün de değerlendirilmesi gerekmektedir.

Bu tez, yüzey merkezli kübik yapıya sahip tek kristal malzemelerin deformasyon mekanizmasını açıklayan ve kristal plastisite kinematığı ve fiziksel temel denklemleri baz alan bir hassas talaşlı imalat modeli sunmaktadır. Sunulan modelde kullanılan temel kanunlar tamamıyla fiziksel olarak ölçülebilen değişkenler üzerinden ifade edilmektedir. Boyut etkisi ilave edilen pekleşme terimi yardımıyla kayma gerinimleri ve kayma düzlemi uzunluğunun bir fonksiyonu olarak modele dahil edilmiştir ve kesme derinliğindeki azalmaya ve dolayısıyla kayma düzlemi boyutundaki azalmaya bağlı olarak, istatistiksel olarak saklanmış dislokasyon miktarında meydana gelen artış üzerinden açıklanmıştır. Bu çalışmada takım radyusu etkisi hesaba katılmamıştır ve gerinim, deformasyon hızı etkisi mevcuttur. Tez kapsamında anlatılan model, optimal kayma açısı değerini bulabilmek için spesifik bir kristal oryantasyonu ve talaşlı imalat parametreleri için deformasyon esnasında yapılan toplam işin minimizasyonu yöntemini kullanmaktadır. Model, Cohen'in Alüminyum ve Bakır tek kristal malzemeler üzerinde yaptığı deneylerde gözlemlenen kuvvet varyasyonlarını yüksek bir korelasyonla açıklayabilmektedir.

## ACKNOWLEDGEMENTS

In the first place, I would like to express my deepest appreciation to my thesis advisor, Assistant Prof. Dr. Eralp Demir, for his patience, motivation, enthusiasm, and immense knowledge. I could not have imagined having a better advisor and mentor for my master study.

I would like to express my sincere gratitude to my committee member Professor Dr. Erhan Budak, for his emotional and motivational support, his precious comments and guiding attitude. As my teacher and mentor, he has taught me more than I could ever give him credit for here. He has shown me, by his example, what a good scientist (and person) should be.

I would like to thank my committee member, Assistant Prof. Dr. Umut Karaguzel for his encouragements and valuable comments.

During the last 2 years of my academic life, my best friend Sefa Mandal was always standing by me to support and encourage me. I would like to thank him for his priceless support. I also thank my dear friends Berna Şensu, Ömer Faruk Sapmaz, and Bora Gönül for all the enjoyable times we shared together.

Finally, I must express my very profound gratitude to my parents Sevgi and Cemil for providing me with unfailing support and continuous encouragement throughout my years of study and through the process of researching and writing this thesis. This accomplishment would not have been possible without them. Thank you.

## TABLE OF CONTENTS

ABSTRACT .....	v
ÖZET .....	vii
ACKNOWLEDGEMENTS .....	ix
LIST OF FIGURES .....	xii
LIST OF TABLES .....	xvi
LIST OF SYMBOLS AND ABBREVIATIONS .....	xvii
1 INTRODUCTION .....	1
1.1 Background of the Study .....	1
1.2 Aims and Objectives .....	6
1.3 Thesis Outline .....	6
Chapter 1 Introduction .....	6
Chapter 2 Literature Review .....	6
Chapter 3 Machining Plasticity Model .....	7
Chapter 4 Numerical Solution Procedure .....	7
Chapter 5 Numerical Results .....	7
Chapter 6 Conclusions and Future Works .....	7
2 LITERATURE REVIEW .....	8
2.1 Strain Rate Effects .....	21
2.2 Size-Effect .....	23
3 MACHINING PLASTICITY MODEL .....	30
3.1 Orthogonal Machining Mechanics .....	30
3.2 Crystal Orientation and Deformation Geometry .....	33
3.3 Single Crystal Deformation Kinematics .....	35
3.4 Physics-Based Single Crystal Constitutive Model .....	38
3.4.1 Dislocation Geometry .....	38

3.4.2	Dislocation Kinetics .....	41
3.4.3	Dislocation Density Evolution .....	48
3.5	Model Constants .....	51
4	NUMERICAL SOLUTION PROCEDURE .....	52
5	NUMERICAL RESULTS .....	54
5.1	Physics Based Model Results .....	54
5.1.1	The effect of Crystallographic Orientation on the Cutting Response .....	54
5.1.2	The effect of Machining Parameters on the Cutting Response .....	56
5.1.3	Size Dependence Results for Planing Simulations .....	60
5.2	Taylor Based Model Results.....	61
5.2.1	The effect of Crystallographic Orientation on the Cutting Response .....	64
5.2.2	The effect of Machining Parameters on the Cutting Response .....	65
5.3	Experimental Validation.....	67
6	CONCLUSIONS & FUTURE WORKS .....	73
6.1	Conclusions .....	73
6.2	Suggestions for the Future Work.....	74
7	REFERENCES .....	75
7.1	Appendix A: Algorithm Flowchart.....	79

## LIST OF FIGURES

Figure 1-1 The schematic representation of the micro-milling process and the physical phenomena parameters that have an influence on the machining response. ....	1
Figure 1-2 The schematic representation of the edge and screw dislocations [31].....	4
Figure 1-3 The schematic representation of Geometrically necessary dislocations underneath an indenter [13] .....	5
Figure 2-1 Schematic representations of the orthogonal cutting on single-crystal workpieces, and the related coordinate systems [19] .....	8
Figure 2-2 Variation of shear angle with rotation angle in (a) crystal A[001] and (b) crystal B[101] [36].....	10
Figure 2-3 Variation of shear angle with rotation angle in (a) crystal A[001] and (b) crystal B[101] [24].....	11
Figure 2-4 The variation of cutting force for various cutting directions in single crystals of Aluminum and Copper, respectively [37] .....	12
Figure 2-5 The variation of cutting forces (a–b) with cutting length obtained by using EMSGCP and EMCP theories and chip shapes (d–e) at cutting length of 2.25 lm for different cutting planes and cutting directions [10] .....	13
Figure 2-6 Definition of the orientation angle for fixed zone axis and sample, crystal, and cutting orientations for the fixed cutting plane experiments, respectively[19] .....	14
Figure 2-7 Experimental validation of the model for aluminum single-crystal machining with fixed zone axis of [0 0 1]: The results for specific cutting energies and shear angle values, respectively. [19].....	15
Figure 2-8 Experimental validation of the model for copper single-crystal machining with fixed zone axis of [0 0 1] [19] .....	15
Figure 2-9 (a) and (b) are the simulated variation and experimental variation in cutting force on (1 1 0) plane, and (c) and (d) presents the simulated variation and experimental variation in cutting force on (1 1 1) plane, respectively [19] .....	16
Figure 2-10 The variation of the surface roughness values with different cutting directions [33] .....	17
Figure 2-11 The variation of the cutting forces with depth of cut values [33].....	17
Figure 2-12 The effect of crystallographic orientation on shear angle[29].....	18
Figure 2-13 The effect of crystallographic orientation on the cutting force and surface roughness, respectively [28] .....	19

Figure 2-14 Variation of cutting forces with crystal orientation in diamond cutting of single-crystal copper when cutting is performed on the (110) and the (111) plane, respectively [38]	20
Figure 2-15 Variation of cutting forces with crystal orientation in diamond cutting of Al single-crystals when cutting is performed on the (110) and the (111) plane, respectively [38]	20
Figure 2-16 Variation of surface roughness with crystal orientation in diamond cutting of Cu single-crystals when cutting is performed on the (110) and the (111) plane, respectively [38]	21
Figure 2-17 Variation of Taylor factor $M'$ (shear strength) with crystal orientation when cutting when cutting is performed on the (110) and the (111) plane, respectively [38]	21
Figure 2-18 The variation of specific cutting energy with or ratio for two edge radii, without considering strain gradient effect [26]	24
Figure 2-19 Variation of specific cutting energy with uncut chip thickness with and without strain gradient (SG) effect [26]	25
Figure 2-20 The schematic representation of the strain gradient model & overall PDZ [16]	26
Figure 2-21 Model of strain gradient: in a row of elements parallel to the shear plane, in a row of elements perpendicular to the shear plane [16]	27
Figure 2-22 Size-effect in the specific shear energy- rake angle of the tool :10 deg[16]	28
Figure 3-1: The schematic representation of orthogonal machining, tool and chip formation	30
Figure 3-2 : The cross-sectional view of the orthogonal machining and cutting forces	31
Figure 3-3 Shear reference (in black color), cutting reference (in red color), rotated-cutting reference (in green color) and crystal reference (in blue color) with $\theta$ : rotation angle about the zone axis, $\phi$ : shear angle	34
Figure 3-4 TEM images of a deformed single crystal [21]	39
Figure 3-5 The schematic representation of the forest dislocation projection of an edge type of dislocation in slip system z onto slip system a.	40
Figure 3-6 $\Lambda$ versus $p(\Lambda) d\Lambda$ , the simplified and the log-normal probability density function for a mean segment length, $\Lambda_0$ , of 10 – 6m.	42
Figure 3-7 Schematic drawing showing internal stress fields during dislocation movement through the crystal lattice [7]	43
Figure 3-8 Schematic sketch of the thermally activated glide process	44
Figure 3-9 Effective stress (MPa) vs. average dislocation velocity (m/s) for thermally-activated glide, viscous drag, and unified rule.	47
Figure 3-10 The schematic representation of the dislocation annihilation [5]	48

Figure 3-11 The schematic representation of the cross-slip mechanism in FCC metals-The sequence of the events a,b,c,d, respectively [15] .....	49
Figure 3-12 : The schematic representation of shear zone and length scale .....	50
Figure 4-1 The schematic representation of Cauchy Stress State, P, at the shear reference frame.....	53
Figure 5-1 Turning of a crystal with cube orientation. $\langle pqr \rangle$ is the crystallographic direction that the crystal is turned around. $\langle pqr \rangle$ corresponds to [001] for cube orientation.....	55
Figure 5-2 Specific cutting energy (MPa) vs. rotation angle $\theta$ (deg.) about the zone axis $\{pqr\}$ $\langle 100 \rangle$ , $\langle 110 \rangle$ and $\langle 111 \rangle$ , respectively .....	55
Figure 5-3 Shear angle (deg.) vs. rotation angle $\theta$ (deg.) about the zone axis $\{pqr\}$ $\langle 100 \rangle$ , $\langle 110 \rangle$ and $\langle 111 \rangle$ , respectively .....	56
Figure 5-4 Effect of friction coefficient, on the cutting constant (MPa) vs. rotation angle $\theta$ (deg.) about the zone axis $\{pqr\}$ .....	57
Figure 5-5 Effect of rake angle on the cutting constant (MPa) vs. rotation angle $\theta$ (deg.) about the zone axis $\{pqr\}$ .....	58
Figure 5-6 Effect of uncut chip thickness values on the cutting constant (MPa) vs. rotation angle $\theta$ (deg.) about the zone axis $\{pqr\}$ .....	59
Figure 5-7 Effect of temperature on the cutting constant (MPa) vs. rotation angle $\theta$ (deg.) about the zone axis of $\langle 100 \rangle$ direction in rate-sensitive single crystal model .....	60
Figure 5-8 Dependence of shear stress on uncut chip thickness values of 15 $\mu\text{m}$ , 20 $\mu\text{m}$ , 25 $\mu\text{m}$ and 30 $\mu\text{m}$ . x axis represents the amount of shear (in radians) along the shear plane.....	61
Figure 5-9 Cutting Constant (MPa) vs. rotation angle $\theta$ (deg.) about the zone axis $\{pqr\}$ $\langle 100 \rangle$ , $\langle 110 \rangle$ and $\langle 111 \rangle$ , respectively.....	64
Figure 5-10 Shear angle (deg.) vs. rotation angle $\theta$ (deg.) about the zone axis $\{pqr\}$ $\langle 100 \rangle$ , $\langle 110 \rangle$ and $\langle 111 \rangle$ , respectively.....	64
Figure 5-11 Effect of friction coefficient, on the cutting constant (MPa) vs. rotation angle $\theta$ (deg.) about the zone axis of $\langle 100 \rangle$ direction in rate-insensitive Taylor-based single crystal model.....	65
Figure 5-12 Effect of rake angle, on the cutting constant (MPa) vs. rotation angle $\theta$ (deg.) about the zone axis of $\langle 100 \rangle$ direction in rate-insensitive Taylor-based single crystal model.....	66
Figure 5-13 Effect of uncut chip thickness, on the cutting constant (MPa) vs. rotation angle $\theta$ (deg.) about the zone axis of $\langle 100 \rangle$ direction in rate-insensitive Taylor-based single crystal model.....	67

Figure 5-14 The variation of the Cutting force for turning a single crystal Aluminum about crystallographic zone axis of $\langle 100 \rangle$ direction for test-3 (Al- $\alpha=40$ deg) and test-8 (Al- $\alpha=50$ deg), respectively. ....	68
Figure 5-15 The variation of the Cutting force for turning a single crystal Copper about crystallographic zone axis of $\langle 100 \rangle$ direction for test-13 (Cu- $\alpha=20$ deg) and test-15 (Cu- $\alpha=40$ deg), respectively. ....	69
Figure 5-16 The variation of the Shear Angle values for turning a single crystal Aluminum about crystallographic zone axis of $\langle 100 \rangle$ direction for test-3 (Al- $\alpha=40$ deg).....	70
Figure 5-17 The variation of the Shear Angle values for turning a single crystal Aluminum about crystallographic zone axis of $\langle 100 \rangle$ direction for test-8 (Al- $\alpha=50$ deg).....	70
Figure 5-18 The variation of the Shear Angle values for turning a single crystal Copper about crystallographic zone axis of $\langle 100 \rangle$ direction for test-13 (Cu- $\alpha=20$ deg).....	71
Figure 5-19 The variation of the Shear Angle values for turning a single crystal Copper about crystallographic zone axis of $\langle 100 \rangle$ direction for test-15 (Cu- $\alpha=40$ deg).....	71

## LIST OF TABLES

Table 2-1 Summary of single crystal micro machining works .....	29
Table 3-1: Slip system for FCC crystals; $s^a$ and $n^a$ denote the slip direction and slip plane normal, respectively, in the crystal reference frame .....	37
Table 3-2 Description and values of constants used in the dislocation-density-based constitutive laws for single crystal simulations.....	51
Table 5-1 Description and both nominal and alternate values of cutting parameters. ....	54
Table 5-2 The machining parameters used in the experiments of Cohen[6].....	67
Table 5-3 Material constants used as model constants for experimental data of Cohen.....	68

## LIST OF SYMBOLS AND ABBREVIATIONS

$\alpha$	rake angle of the cutting tool
$\beta$	friction angle between cutting tool and chip
$\sigma^c, \{\sigma^c\}$	Bishop-Hill stress tensor and its vectorized form
$\sigma$	Cauchy stress tensor on the shear plane
$X_z^\alpha$	dislocation interaction matrix between slip systems z and a
$\Delta F$	thermal activation energy required for slip
$\Delta G$	activation energy required for slip
$\dot{\gamma}^a$	slip rate of slip system a
$\dot{\rho}^a$	evolution rate of dislocation density on slip system a
$\dot{\rho}^a$	evolution rate of total dislocation density on slip system a
$\dot{W}_C$	cutting power
$\dot{W}_f$	friction power
$\dot{W}_{tot}$	total power
$\gamma$	total amount of shear
$\dot{\mathbf{F}}^P$	time rate of change of plastic deformation gradient
$\hat{\mathbf{C}}$	cubic elasticity matrix at the intermediate configuration
$\hat{\mathbf{n}}^a$	slip plane normal of slip system a at the intermediate configuration
$\hat{\mathbf{P}}$	2nd Piola-Kirchoff stress tensor
$\hat{\mathbf{p}}$	vectorized 2nd Piola-Kirchoff stress
$\hat{\mathbf{S}}^a$	Schmid tensor of slip system a at the intermediate configuration
$\hat{\mathbf{s}}^a$	slip direction of slip system a at the intermediate configuration
$\mathbf{C}$	cubic elasticity matrix at the crystal frame
$\mathbf{E}^e$	Green-Lagrange strain tensor
$\mathbf{e}^e$	vectorized Green-Lagrange strain components
$\mathbf{F}^e$	elastic part of the deformation gradient
$\mathbf{F}^P$	plastic part of the deformation gradient
$\mathbf{F}$	deformation gradient
$\mathbf{L}^P$	plastic part of the velocity gradient
$\mathbf{n}^a$	slip plane normal of slip system a at the crystal frame

<b>R</b>	overall transformation matrix from shear frame to crystal frame
<b>s<sup>a</sup></b>	slip direction of slip system a at the crystal frame
<b>S</b>	shear plane dyadic
<b>t<sup>a</sup></b>	line direction of edge type dislocations on slip system a at the crystal frame
<b>T<sub>c→cr</sub></b>	transformation from cutting frame to crystal frame
<b>T<sub>sh→c</sub></b>	transformation from shear frame to cutting frame
<b>μ</b>	friction coefficient between the rake face of the cutting tool and chip
<b>v<sub>D</sub></b>	Debye frequency
<b>∅</b>	shear angle of the shear plane
<b>ρ</b>	mass density
<b>τ<sup>*</sup></b>	short-range obstacle strength
<b>τ<sup>a</sup></b>	resolved shear stress at slip system a at the intermediate configuration
<b>τ<sub>μ</sub><sup> α </sup></b>	long-range obstacle strength
<b>θ</b>	rotation angle about the given zone axis {pqr}
<b>ρ<sup>a</sup></b>	primary dislocation density at slip system a
<b>ρ<sub>0</sub></b>	initial dislocation density
<b>ρ<sub>f</sub><sup>a</sup></b>	forest dislocation density at slip system a
<b>ρ<sub>m</sub><sup>a</sup></b>	mobile dislocation density of slip system a
<b>{pqr}</b>	crystallographic zone axis about which the crystal is turned
<b>A, B, C, F, H, I</b>	Bishop-Hill stress constants
<b>a<sub>s</sub></b>	area of the shear plane
<b>b</b>	Burgers vector
<b>B<sub>0</sub></b>	drag coefficient
<b>c<sub>1</sub></b>	mean-free-path scaling constant for forest dislocation spacing
<b>c<sub>2</sub></b>	geometric constant for the long range flow stress
<b>c<sub>3</sub></b>	adjusting parameter for jump distance
<b>c<sub>4</sub></b>	mean-free-path hardening constant
<b>c<sub>5</sub></b>	temperature and strain-rate dependent annihilation constant
<b>c<sub>6</sub></b>	length-scale dependent dislocation density scaling constant
<b>c<sub>s</sub></b>	shear wave speed
<b>C<sub>11</sub>, C<sub>12</sub>, C<sub>44</sub></b>	cubic elasticity constants
<b>d<sup>a</sup></b>	mean-free-path of slip system a
<b>f</b>	friction force on the rake face of the cutting tool

$f_c$	cutting force (along cutting direction)
$f_n$	normal force on the shear plane
$f_s$	shear force on the shear plane
$f_t$	tangential force (normal to machined surface)
G	shear modulus
$i_0$	self-dislocation interaction coefficient
$i_1$	co-planar dislocation interaction coefficient
$i_2$	cross-slip dislocation interaction coefficient
$i_3$	glissile dislocation interaction coefficient
$i_4$	Hirth dislocation interaction coefficient
$i_5$	Lomer-Cottrell dislocation interaction coefficient
K	Boltzman Constant
$K_c$	cutting constant
L	length of the shear plane
$l_f$	mean spacing between forest dislocations
n	normal force on the rake face of the cutting tool
q	number of atoms per unit cell
r	resultant force
$r(\tau^a, \rho_f^a)$	fraction of mobile dislocation density of slip system a
T	temperature
$t_0$	uncut chip thickness
$t_w$	average dwell time of dislocation in-front of an obstacle
v	cutting speed
$V^a$	activation volume of slip system a
$v^a$	average dislocation velocity of slip system a
$v_c$	chip flow speed
$v_s$	shearing speed on the shear plane
$v_d^a$	average viscous drag velocity of slip system a
$v_{th}^a$	average thermally activated velocity of slip system a
w	width of cut
$W_{tot}$	total work

# 1 INTRODUCTION

## 1.1 Background of the Study

It has been known that micromachining is an emerging field that has shown potential to produce complex shapes at small scales with acceptable dimensional accuracy and its applicability to wide-range of materials. These attributes command an ever-increasing attention to the modeling of this process. The accuracy of the process and the cutting response are affected by numerous factors, such as machining parameters and the workpiece properties. There have been many studies which try to model the effect of process parameters such as cutting speed, tool's rake angle, edge radius, cutting speed, depth of cut etc. on the cutting response of metals. However, a fundamental understanding is needed for explaining the material's length scale and crystal orientation dependent behavior.

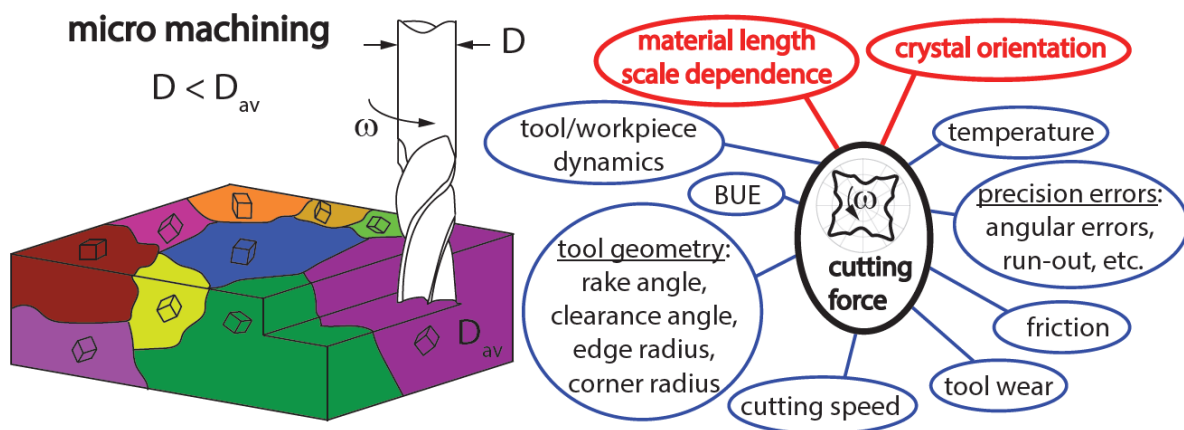


Figure 1-1 The schematic representation of the micro-milling process and the physical phenomena parameters that have an influence on the machining response.

Figure 1-1 indicates the important factors that affect the cutting force during machining process. In the aspect of micro-machining, the tool-workpiece interaction occurs entirely within either a single crystal or a few crystals. As a result, it becomes more important to both incorporate the crystallographic effects as well as size-effects to the machining plasticity models.

Orthogonal cutting is the simplest cutting geometry, thereby studying orthogonal cutting geometry allows understanding of the effect of parameters other than cutting geometry in a more direct way. The proposed methodology can be extended to the oblique cutting geometries can be done easily with the geometrical model of the particular machining process.

In orthogonal cutting, machining is divided into mainly three different zones. Primary zone is the shear plane where shearing deformation is dominant. As the edge of the tool penetrates into the workpiece, the material ahead of the tool is sheared over the primary shear zone to form a chip. Secondary zone refers to the region between the cut (machined) workpiece surface and the friction face of the cutting tool. In other words, the chip partially deforms and moves along the rake face of the tool, which is called secondary deformation zone. Third zone where the flank of the tool rubs the newly machined surface, is called the tertiary zone. Since the shearing deformation is dominant on the primary shear zone, this region is considered when modeling the size-effect.

The polycrystalline material can be considered as the aggregate of several crystals or grains and the boundary between the grain is the grain boundary across which the orientation of the crystal changes. Therefore, single crystal material can be defined as a material in which the crystal lattice of the entire sample is continuous with no grain boundaries. The absence of the grain boundaries has an importance because it gives single crystal materials unique properties particularly mechanical, optical and electrical, which can also be anisotropic, depending on the type of crystallographic structure. They are useful for applications where grain boundaries are harmful. For example, high temperature deformation or creep resistance and Ni-based single crystal superalloys are widely used in aerospace industry due to this unique property. Another important point is that, in a single crystal, the physical and mechanical properties change with orientation. This is due to the easiness of the movement of atoms (slip or distortion) in some directions than others which results in the changing material properties with different crystallographic orientations, or in another way of saying anisotropy of the material. When it comes to the polycrystalline materials, even if the individual grains are anisotropic, the property

differences tend to average out due to the randomness of the grain orientations. Therefore, the material is isotropic until the material is formed where the grains are distorted and elongated.

Anisotropy can be explained in two parts: elastic and plastic anisotropy. The elastic anisotropy of crystalline material arises from the directionality of the electronic bond and the resulting crystal lattice structure. The plastic anisotropy of crystalline matter also departs from the directionality of the electronic bond and the resulting crystal lattice structure. Both aspects determine which slip planes and which Burgers vectors serve for the motion of lattice dislocations or the activation of plastically relevant athermal transformations. The elastic anisotropy is determined by the crystal texture, whereas the plastic anisotropy is determined by the microstructural parameters like dislocation density and grain boundary. The importance of plastic anisotropy is that metals are deformed in a discrete rather than in a continuum fashion. In addition to the anisotropy or macroscopic anisotropy, there is also anisotropic behavior of the single crystal which results from the crystallographic nature of plastic glide, interactions between the glide systems and eventually anisotropy of elastic constants.

This study focused on examining the behavior of single crystal materials during machining since characteristic dimensions of grains in metals becomes comparable with the uncut chip thickness values experienced in micromachining and the process takes place within individual grains which exhibits elastic and plastic anisotropy and a few grains at a time. Therefore, the mechanical properties change when crossing into different grains which leading to changes in the magnitude and direction of the cutting force rake and flank-face friction, as well as amount of elastic recovery during the process. Unlike the macroscale cutting processes, where a large number of grains are encountered and the material can usually be assumed to behave isotropically.

The plastic deformation in metals can be attributed to the movement of large numbers of atoms in response to an applied stress. Dislocations can be defined as a boundary between deformed and undeformed regions in the crystalline structure. Slip motion of the dislocations can be explained as the sliding displacement along a plane of one part of a crystal relative to the rest of the crystal due to the shearing forces. Plastic deformation of materials under stress is the

result of slip within the individual crystals that constitute the material. Slip and the twinning, are the only ways that crystals in solids can be permanently deformed. In slip, all the atoms on one side of the slip (or glide) plane do not slide simultaneously from one set of positions to the next. The atoms move sequentially one row at a time into the next position along the plane because of structural defects or spaces, called edge dislocations, in the crystal that move at the same rate in the opposite direction. Direction and magnitude of slip is characterized by the Burgers vector of the dislocation. There are two basic types of dislocations which are characterized by the relative orientation between the Burgers vector and dislocation line. Figure 1-2 shows the schematic representation of the edge and the screw dislocations. To be conclude, an edge dislocation also can be defined as localized lattice distortion exists along the end of an extra half-plane of atoms whereas a screw dislocation results from shear distortion. As can be seen in the figure, for an edge dislocation, the Burgers vector is parallel to dislocation motion and for a screw dislocation, the Burgers vector is parallel to the dislocation and it is always parallel to slip.

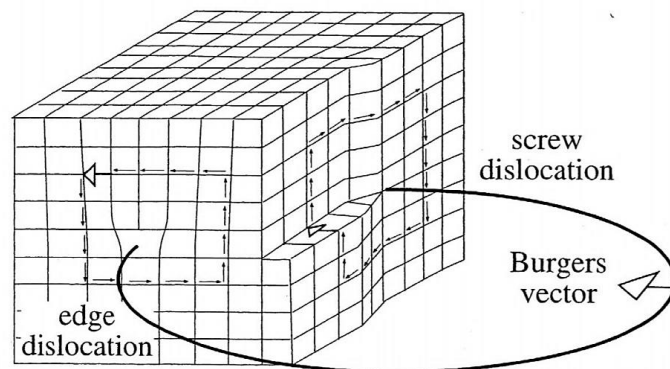


Figure 1-2 The schematic representation of the edge and screw dislocations [31]

An important feature of the micro-machining is the presence of the size-effect which is the non-linear increase in specific cutting energy inherent to the material and it may occur due to some differences which may be related with tool edge radius, workpiece non-homogeneity with respect to the tool/cut size, negative rake angles and workpiece material minimum chip thickness effects. In the aspect of workpiece homogeneity such as crystallographic defects such as grain boundaries, missing and impurity atoms, etc. these factors could cause an increase in material strength, since the deformation takes place in a small volume. In another explanation which is related with tool edge radius, the increase in specific cutting force with decrease in uncut chip thickness is explained by ploughing force arising from frictional rubbing and

ploughing associated with material removal by a blunt tool. Moreover, any changes in tool edge radius can cause change in shear angle values and effective rake angle of the tool and this also can be considered as another explanation for the size-effect. Finally, size-effect can be explained by considering the strain gradient plasticity theory. By using this theory, strength of material is considered as a function of the strains and strain gradients as well. In order to explain the presence of a strain gradient in the strain field, geometrically necessary dislocations are needed in addition to statistically stored dislocations to accommodate them.

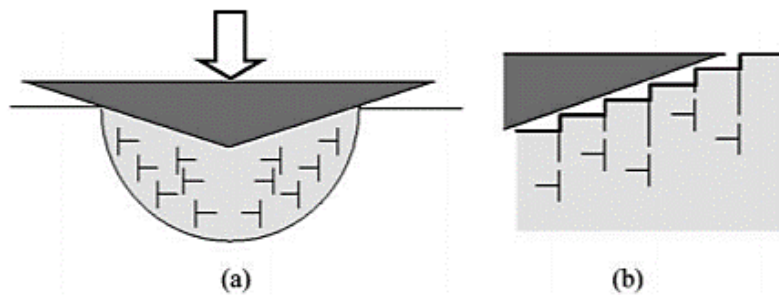


Figure 1-3 The schematic representation of Geometrically necessary dislocations underneath an indenter [13]

In case of non-uniform plastic deformation, there will be an extra storage of geometrically necessary dislocations (GND) and these defects show their effects when the length of deformation is sufficiently small. Figure 1-3 above explains the formation of geometrically necessary dislocations underneath an indenter. (a) represents the mechanism of creating extra storage of defects by pushing substrate material and (b) shows the atomic steps on the indented surface and the associated geometrically necessary dislocations, respectively. Due to the reduction in the shear plane length, an increase in the shear strain gradients and in the density of geometrically necessary dislocations increases compared to the density of statistically stored dislocations, which leading to an increase in shear strength. It is the possible explanation of the size-effect occurrence in a strain field based on its geometry and gradient. By using a strain gradient plasticity-based model of material deformation in the Primary Deformation Zone of an orthogonal cutting process and formulations of the strain gradient, density of geometrically necessary dislocations, shear strength of the material in the PDZ and the specific shear energy, the size-effect can be modeled in a more realistic way compared to other explanations presented above.

In single-crystal machining processes, these differences and associated effects should be carefully examined, and more-realistic material models should be created. The review of literature indicates that there are some studies for single-crystal machining which was considered these aspects, but they partly cover size-effect and crystal orientation.

## **1.2 Aims and Objectives**

The aim of this research is to develop a physics-based model for the micro-machining process of FCC single crystals to explain crystal orientation and size dependence of cutting forces. To achieve this goal :

- The shear angle is computed by minimization of total work that is necessary to shear the crystal.
- Cutting force signatures during turning of a single crystal along different crystallographic direction is computed to illustrate the amount and periodicity of force fluctuations due to crystallographic origins.
- The effect of depth of cut dependence is computed including the strain-rate effects.
- The method is applied to reproduce experimental force fluctuations of Aluminum and Copper single crystals in Cohen's work. This includes calibration of the model to find appropriate model constants.

## **1.3 Thesis Outline**

### **Chapter 1 Introduction**

This chapter aims the giving an insight about the background and scope of this research, and presents overview of knowledge and some important points which forms a basis for the thesis.

### **Chapter 2 Literature Review**

This chapter defines the level of the on-going research relating the single crystal machining and size-dependence effects on the machining processes by provide an overview of past and on-going researches on this issue.

### **Chapter 3 Machining Plasticity Model**

This chapter includes three main parts: in the first part, mechanics of the orthogonal machining process and related force and velocity expressions are shown. In the 2<sup>nd</sup> part, single crystal orientation and deformation geometry and related expressions are derived special to machining process. In the 3<sup>rd</sup> part, single crystal deformation kinematics formulations are provided. Finally, the 4<sup>th</sup> part includes the single crystal constitutive laws.

### **Chapter 4 Numerical Solution Procedure**

This chapter explains the numerical solution procedure and the algorithm used in the model.

### **Chapter 5 Numerical Results**

This chapter consisting of two main parts: in the first part, the simulation results of the physics-based model are discussed. In the 2<sup>nd</sup> part, the results of the Taylor based Model are given. Finally, the last part includes experimental validation of the simulation results.

### **Chapter 6 Conclusions and Future Works**

This chapter presents the conclusions of the research described in the thesis. The aim and objectives of the research, outlined in chapter 1, are reviewed and their achievement addressed.

## 2 LITERATURE REVIEW

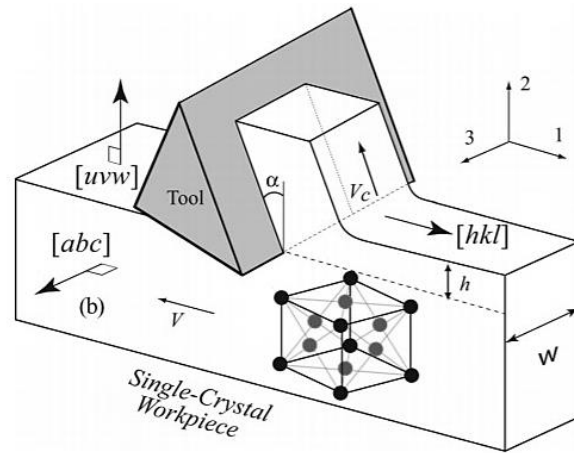


Figure 2-1 Schematic representations of the orthogonal cutting on single-crystal workpieces, and the related coordinate systems [19]

In machining processes, the experimentation methods and techniques are expensive and time-consuming. Therefore, there is an increasing trend towards developing the numerical computation methods and analytical models to analyze the process. In single crystal micromachining processes, many differences are observed in the aspect of both process conditions and also material-related effects compared to classical macro-machining processes. One of the most important material related effect that has to be considered is the material anisotropy. The importance of material anisotropy or crystallographic orientation stem from the nature of the micro-machining process where the tool-workpiece interaction occurs within a single or a few crystals. Therefore, investigating the relation between the anisotropy and cutting forces, afterwards incorporating the anisotropy into the micro-machining models still maintains its importance. Figure 2-1 above, shows the schematic representations of the orthogonal cutting operation on single-crystal workpieces. The analytical models are sub-categorized with respect to rate dependency. The rate insensitive plasticity models include Schmid based iso-stress models and Taylor iso-strain models. In these models, Schmid factor and Taylor factor are used to relate the yield stress with the critical resolved shear stress on each slip systems. In Schmid based models, or Sachs model, it is assumed that all single crystals grains with aggregate experience the same state of stress and equilibrium condition across the grain boundaries are satisfied whereas compatibility across grains is violated. Moreover, in each grain, deformation

takes place by single slip on the most highly stressed slip system, i.e. the one with the highest Schmid factor which is used to predict the active slip systems. Ueda and Iwata [36], examine the chip formation mechanism on the single crystal  $\beta$ -brass. They used Schmid factor to estimate the shear angle theoretically with assuming the axis of applied load to the crystal coincides with the direction of the resultant cutting force. Moreover, they found that there is a good agreement between the measured shear angle value and the theoretical one which is calculated based on the Schmid factor analysis of the active slip system (110)  $\langle 111 \rangle$  also by considering the role of downward slip system. Finally, they concluded that there are some favorable cutting directions with respect to crystallographic orientation which improves the surface roughness significantly.

Taylor models which is proposed by Taylor and later derived in detail by Bishop and Hill, assumed that all single-crystal grains within the aggregate experience the same state of deformation or strain and compatibility conditions between the grains satisfied. Lee and Zhou [24], analyzed the effect of crystallographic orientation on chip formation theoretically by using a microplasticity model which is based on the minimum effective Taylor factor. They came to a conclusion that the previous studies examining shear angle predictions by using Schmid based models, the absolute values and trends were different and also predicted cyclic variation in shear angle was found to be out of phase with the measured values compared to experimental data. The variation in shear angle values with rotation angle in crystal A [001] and crystal B[101] from the work Ueda and Iwata, is presented in the figure 2-2, below.

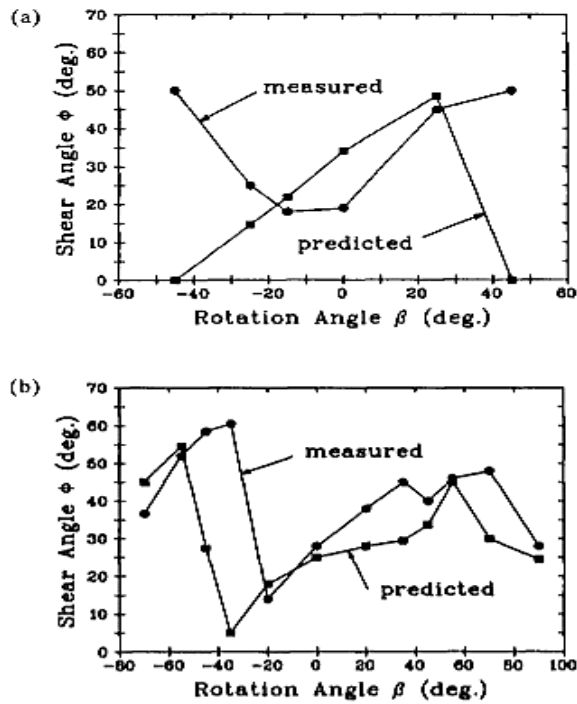


Figure 2-2 Variation of shear angle with rotation angle in (a) crystal A[001] and (b) crystal B[101] [36]

However, their microplasticity model which is based on the Taylor factor, could predict a range of shear angle values for a given state of material anisotropy. Taylor factor is a dimensionless number sensitive to the crystallographic orientation and it is calculated by considering the maximum work principle of Bishop and Hill. According to their model, the variation in shear angle values with rotation angle in crystal A[001] and crystal B[101] is presented in the figure 2-3, below.

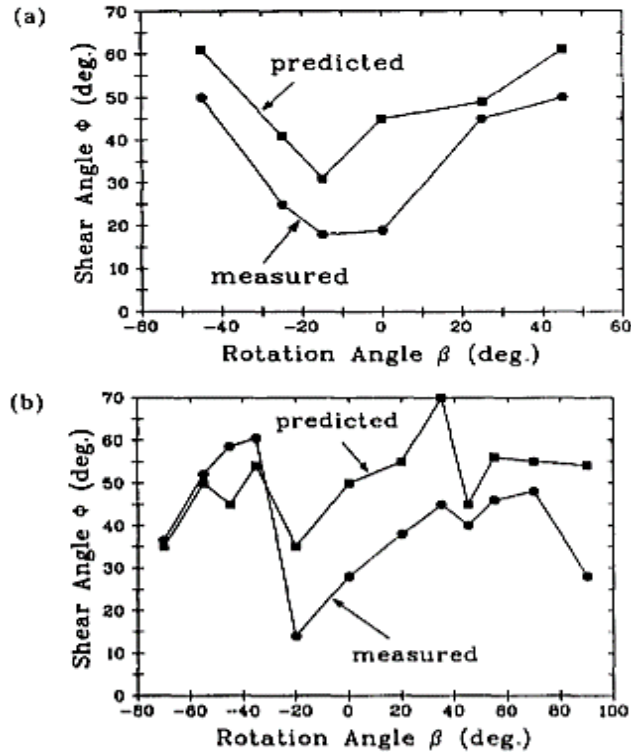


Figure 2-3 Variation of shear angle with rotation angle in (a) crystal A[001] and (b) crystal B[101] [24]

Finally, they found a good agreement between the theoretical shear angle values and experimental data to model the effect of crystallographic cutting direction on the shear angle by using microplasticity model of shear band formation. Another important finding of this study is that by using the change in the crystallographic orientation of the material with respect to the cutting direction, the pattern of variation in cutting forces can easily be predicted.

It should be noted that to produce the specified amount of strain in Taylor models, 5 slip systems are needed to be active and the selection of these slip systems for FCC metals which have 12 slip systems is not unique. As can be understood from the explanations given above, there are some problems associated with the usage of these models which could be summarize as determination of active slip systems, and the increments of shear on active systems.

Afterwards, the crystal plasticity finite element models gained momentum. It is known that the deformation processes in real-life are more complex and it is required to consider more than

one active slip system at each incremental deformation, on the contrary to early modelling approaches. As a result, there is a need of comprehensive modelling frameworks to analyze the cutting forces and stresses. In finite element models, the entire volume under consideration is discretized into the elements and the velocity gradient is written in dyadic form. These models have also evolved to employ some of the extensive knowledge gained from experimental and theoretical studies of single-crystal deformation and dislocations. Although there are some studies which is used molecular dynamic (MD) simulations to study the chip removal mechanism, due to the required amount of computational power to model the deformation in physically meaningful volumes, FE/SPH models are more preferred. Zahedi et al. [37] used a hybrid modelling approach which includes both smoothed particle hydrodynamics and continuum finite element analysis to model the variation of cutting forces in machining of FCC single crystals. They conducted simulations by considering orthogonal cutting mechanism on the Al and Cu single crystals.

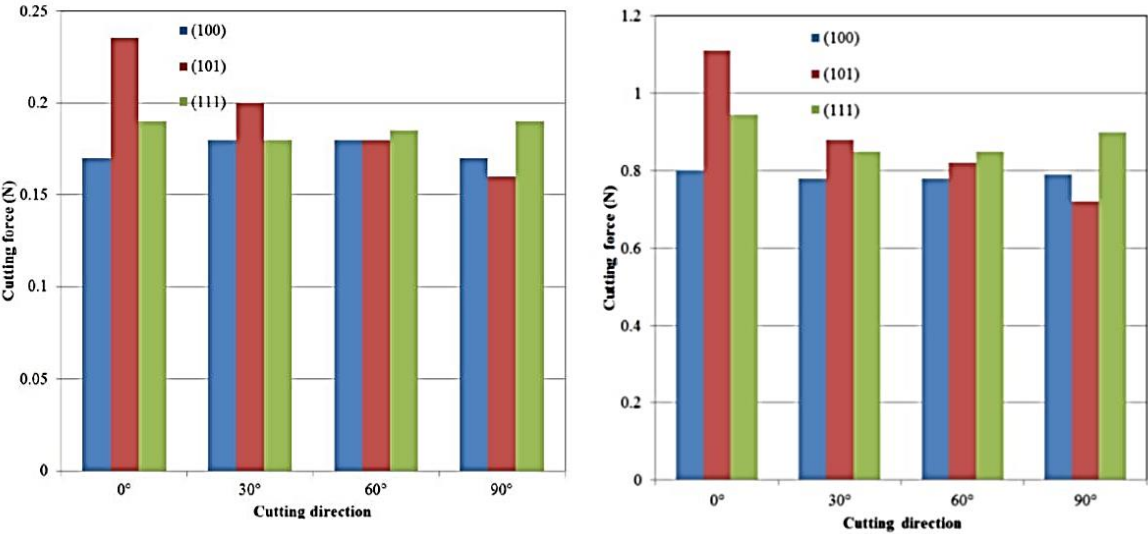


Figure 2-4 The variation of cutting force for various cutting directions in single crystals of Aluminum and Copper, respectively [37]

As it can be seen in the Figure 2-4, they found that the magnitude of the cutting force values were different in aluminum and copper when cutting realized under the same conditions; however, the character of variation of the cutting force for different orientations for both materials was similar. They also concluded that chip morphologies after machining also shows

similarity in the type of chip formed for copper and Aluminum which leading to the conclusion that the nature of the deformation significantly affected by the orientation and direction of cutting.

In another study, Demiral et al. [10] investigate the underlying micromechanics of micromachining process, by using a 3D finite-element model of orthogonal micro-machining of FCC single crystal copper. They conducted simulations by considering different types of strain gradient crystal plasticity theories and conventional crystal plasticity theory. In EMCP theory, they did not consider the GNDs evolving in the course of deformation. However, in EMSGCP theory, the contribution of the evolution of the GNDs to local hardening of the material was considered.

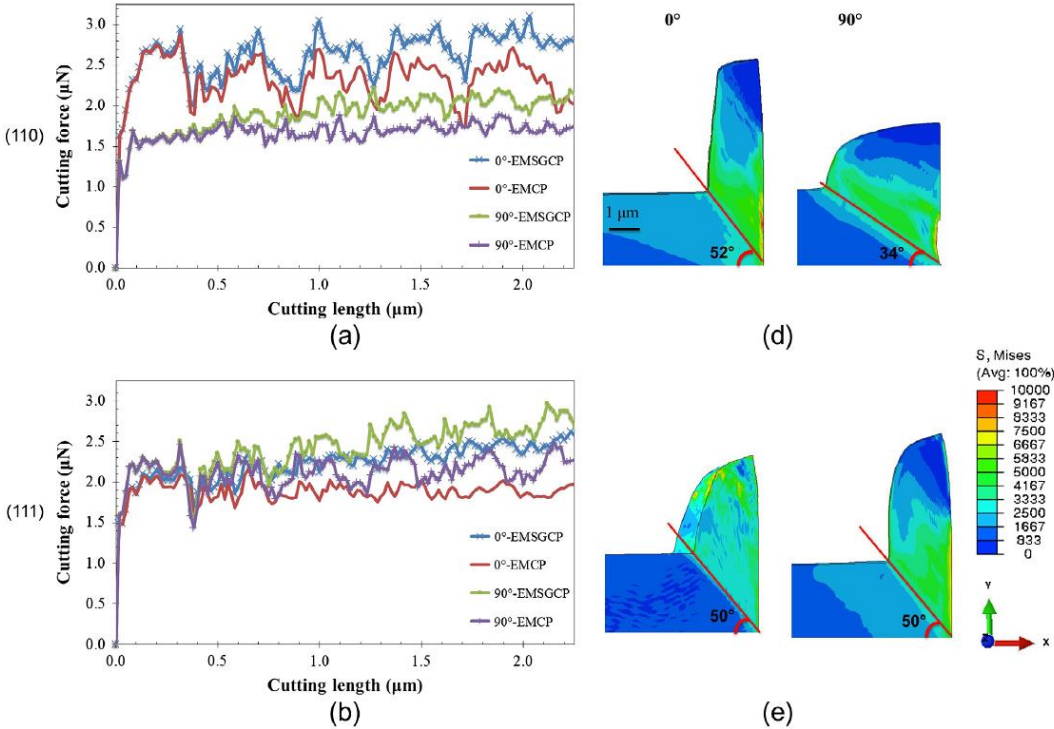


Figure 2-5 The variation of cutting forces (a–b) with cutting length obtained by using EMSGCP and EMCP theories and chip shapes (d–e) at cutting length of 2.25  $\mu\text{m}$  for different cutting planes and cutting directions [10]

According to their results, in the figure 2-5 above, EMSGCP theory predicts a cutting force that increases with an increase in the cutting length; in contrast to the EMCP theory. They concluded

that this difference between two theories was due to the strain-hardening rate since EMSGCP theory accounting for the evolution of strain gradients during deformation. Finally, they combined crystal plasticity kinematics with a strain gradient hardening term; therefore, the model was able to capture the size-effect in machining problems successfully. Their simulations showed that the EMSGCP theory is able to capture average cutting energy obtained in good agreement with experimentally obtained value of specific cutting energy for all crystal orientations and cutting directions.

The finite element models do not maintain its popularity due to the long computational times and high cost values associated with these tools. The deformation in machining process involves both frictional contact and chip formation and the finite element models are not considered the best way to model the process. Finally, more recent efforts in this field, focused on physically based models. Kota et al. [19] developed a crystal-plasticity based model to investigate the effect of crystallographic orientation, friction and the cutting geometry on the cutting response for orthogonal cutting of FCC single-crystal metals. The plasticity-based machining model which includes Bishop and Hill’s crystal plasticity theory and Merchant’s machining force model is used to determine optimal shear angle solution by minimizing total work over allowable shear angles. They also provide an experimental validation using data from the literature for both single-crystal aluminum and single-crystal copper and by considering both varying cutting direction for constant zone axis, and for varying zone axis for constant cutting plane conditions. The schematic representation of the first and the second part of the experimental validation where a disk-type workpiece is considered in plunge-turning configuration, is presented in the figure 2-6 below.

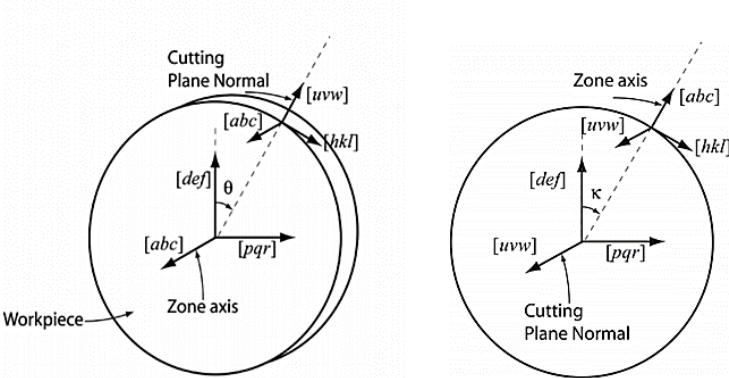


Figure 2-6 Definition of the orientation angle for fixed zone axis and sample, crystal, and cutting orientations for the fixed cutting plane experiments, respectively[19]

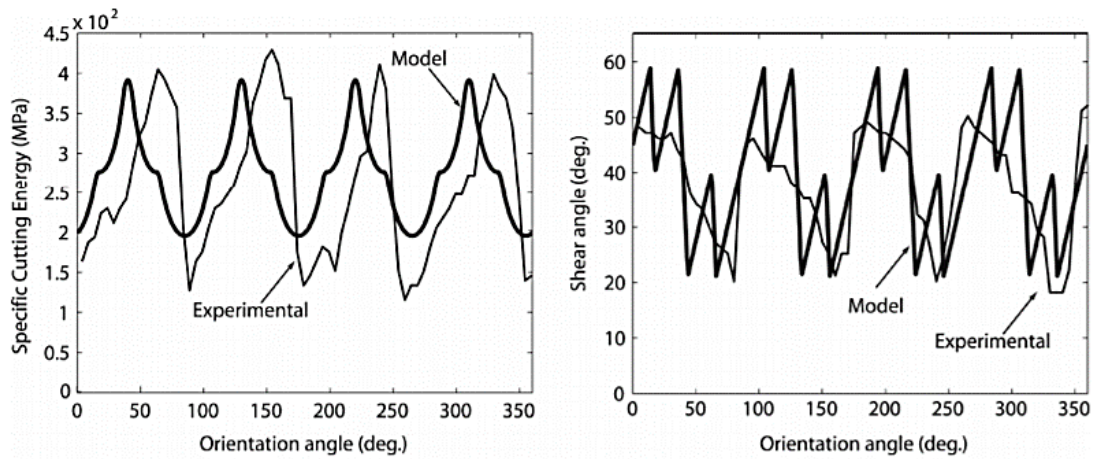


Figure 2-7 Experimental validation of the model for aluminum single-crystal machining with fixed zone axis of  $[0\ 0\ 1]$ : The results for specific cutting energies and shear angle values, respectively. [19]

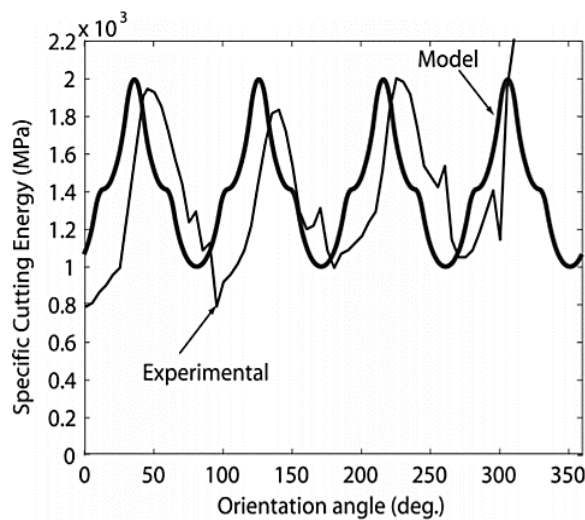


Figure 2-8 Experimental validation of the model for copper single-crystal machining with fixed zone axis of  $[0\ 0\ 1]$  [19]

In the first part of the work, the experimental data presented by Cohen [6] from in-situ diamond-turning experiments on single-crystal aluminum and copper are used. As can be seen in the Figure 2-7 and 2-8 above, they obtained a good match between the model predictions and experimental data, which indicates the model's capability to capture crystallographic anisotropy and symmetry. The second part of the experimental validation includes varying zone axis for fixed value of cutting plane normal. The experimental data presented by Zhou and Ngoi [38]

from planing of single-crystal copper, where different cutting directions on the (1 1 0) and (1 1 1) cutting planes were considered is used for validation.

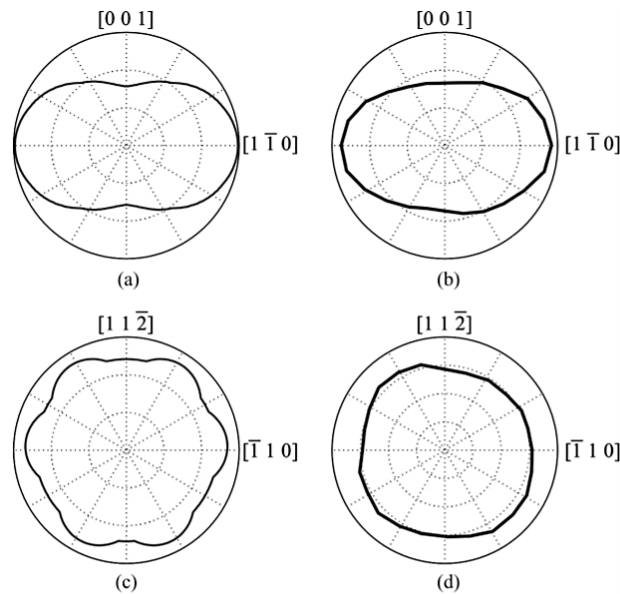


Figure 2-9 (a) and (b) are the simulated variation and experimental variation in cutting force on (1 1 0) plane, and (c) and (d) presents the simulated variation and experimental variation in cutting force on (1 1 1) plane, respectively [19]

Figure 2-9 shows that the model is capable of capturing the force fluctuations on both planes. The variation on the (1 1 0) plane is larger than the variation on (1 1 1) plane. It could be explained by the higher symmetry on (111) plane compared to (110) plane.

Sato et al. [33] investigated the relation between the accuracy of the finished surfaces and the crystallographic orientation, by using their tentatively manufactured ultraprecision machine, and they studied characteristics of the micromachining of Aluminum single crystals. As can be seen in the figure 2-10 below, they found that the cutting in the  $[0\bar{1}1]$  direction achieved the lowest surface roughness value, whereas cutting in the  $[1\bar{2}1]$  direction gives the max value. Therefore, it can be said that cutting direction and their location with respect to sliding surface or direction affects the both roughness and the flatness of the material which helps to explain the importance of controlling specimen orientation effect on the improving working accuracy.

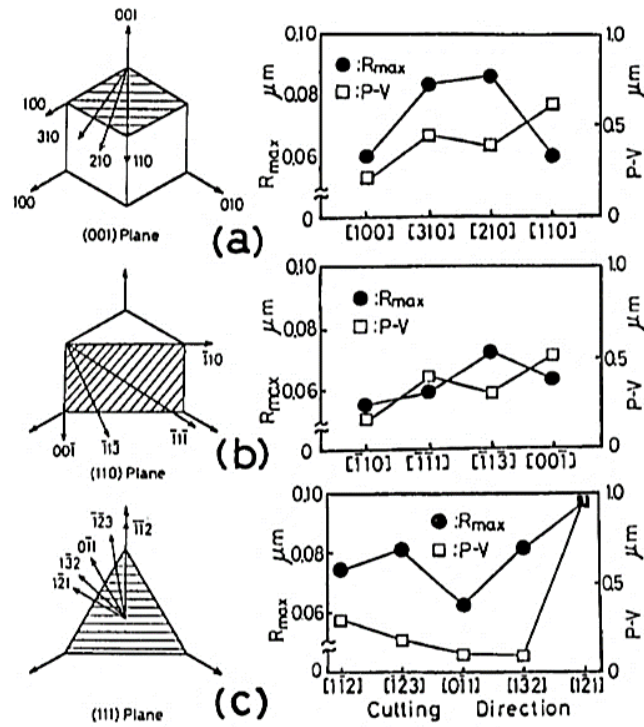


Figure 2-10 The variation of the surface roughness values with different cutting directions [33]

The figure 2-11 indicates that when the depth of cut value reaches  $1.0\mu\text{m}$ , the gradient of the  $F_h$  changes which means that there is a change in cutting mechanism. Therefore, as a second experimental finding, they also shed light the relation between the size-effect and the depth of cut and it can be said that the size-effect occurs when the depth of cut value reached  $1.0\mu\text{m}$  with respect to their setting.

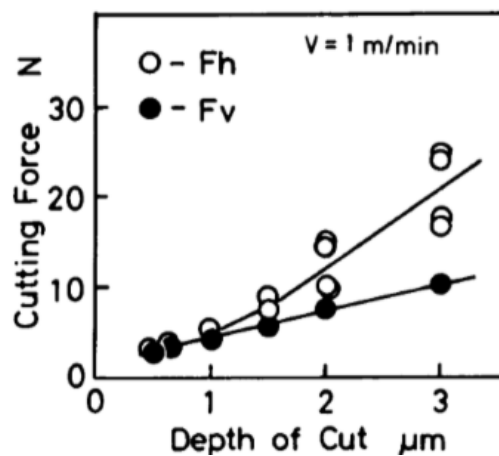


Figure 2-11 The variation of the cutting forces with depth of cut values [33]

In another experimental work, Moriwaki et al. [29] examined the effects of crystallographic orientation on chip formation, cutting force, and surface integrity during micromachining of single crystal Copper and they found that crystallographic orientation has a significant effect on the nominal shear angle when the depth of cut is greater than  $1\ \mu\text{m}$ . The variation of shear angle with crystallographic orientation for different depth of cut values is plotted in the figure 2-12, below.

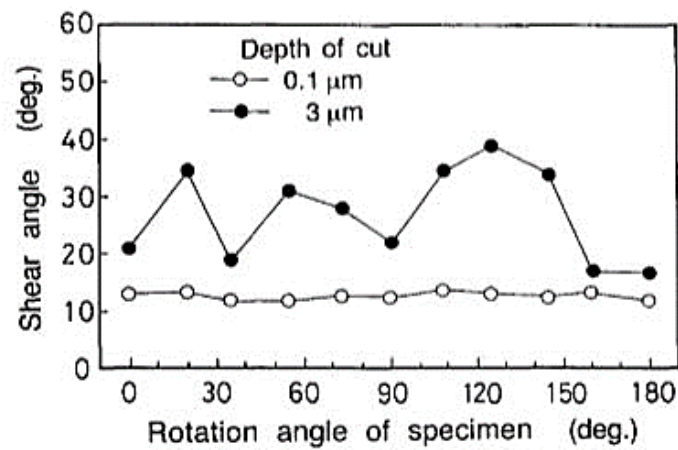


Figure 2-12 The effect of crystallographic orientation on shear angle[29]

Moreover, they observed the same effect on the cutting force and the surface roughness. As it is evident from the figure 2-13 below, the variation in the principal force with the orientation can be considered as opposite to that of shear angle. The variation in the principal force is more dominant when the depth of cut is greater than  $1\ \mu\text{m}$ . They concluded that the reason why the cutting force and shear angle are not significantly affected by the crystallographic orientation is that depth of the damaged layer in this study, reaches  $0.2$  to  $0.5\ \mu\text{m}$ . As a result, when the depth of cut is kept small, the damaged layer is cut.

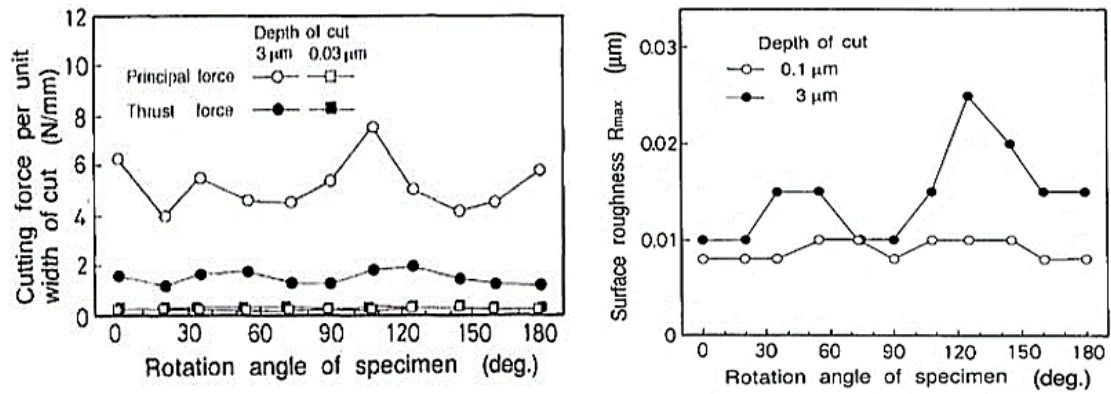


Figure 2-13 The effect of crystallographic orientation on the cutting force and surface roughness, respectively [28]

In one of the other experimental studies, To et al. [35] found that (100) cutting plane gives the best surface finish while the (110) cutting plane results in highest surface roughness during micromachining of Aluminum single crystals, hence these results make it clear that incorporating material anisotropy in micromachining processes is beneficial not only for energy consumption (through determination of cutting forces) but also for quality of the last product and the efficiency of the process.

Ngoi and Zhou [38], investigated the effect of both tool and workpiece orientation on cutting forces and surface roughness during diamond turning of Aluminum and Copper. In the aspect of tool orientation, they measured the variation of friction coefficient and also shear angle and they concluded that workpiece materials are sensitive to the orientation of the diamonds that's the reason why friction coefficient changes with different planes and also along different directions on the same plane. Furthermore, as is evident from the figure 2-14 below, the cutting forces change considerably with orientation of the workpiece and the lowest and highest force values are obtained along  $[1\bar{1}0]$  direction and  $[001]$  direction while cutting is realized on the (110) cutting plane, respectively. The fluctuations in the magnitude of the cutting forces is greater while cutting is performed on the (110) plane.

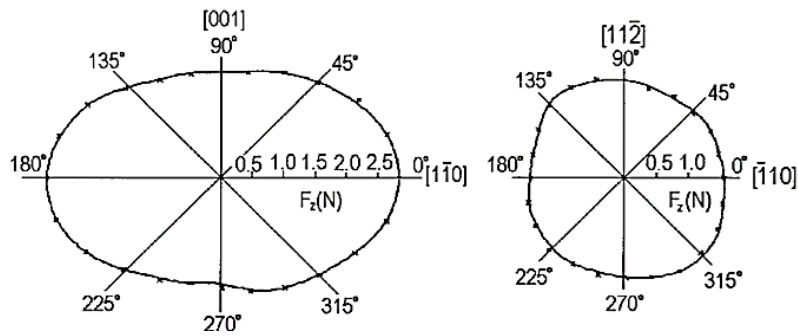


Figure 2-14 Variation of cutting forces with crystal orientation in diamond cutting of single-crystal copper when cutting is performed on the (110) and the (111) plane, respectively [38]

Similarly, figure 2-15 shows the variation of the cutting forces with orientation in diamond cutting of single crystal aluminum. The observed trend in the variation of cutting forces is the same with that observed in the diamond cutting of single-crystal copper.

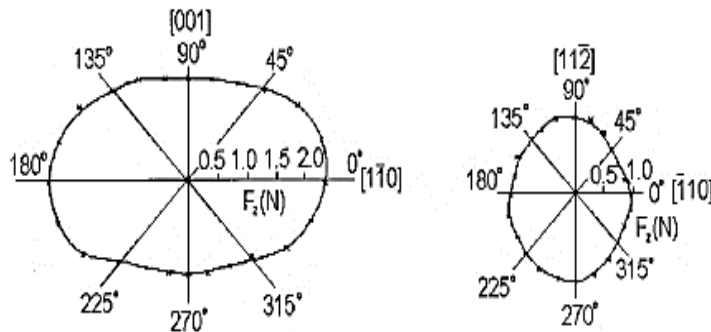


Figure 2-15 Variation of cutting forces with crystal orientation in diamond cutting of Al single-crystals when cutting is performed on the (110) and the (111) plane, respectively [38]

The effect of crystallographic cutting direction on the machined surface roughness was also investigated. As might be seen in the figure 2-16 below, the fluctuations observed in surface roughness is bigger for the case of cutting on the (110) plane which corresponds to higher variation in cutting forces. However, for the case of cutting on the (111) the fluctuations observed in surface roughness is small and it leads to the conclusion that the variation in the cutting forces is not the dominant reason to determine the change in the surface roughness. In order to examine the surface roughness of the machined surface, the elastic and plastic anisotropy of crystalline materials also has to be taken into account.

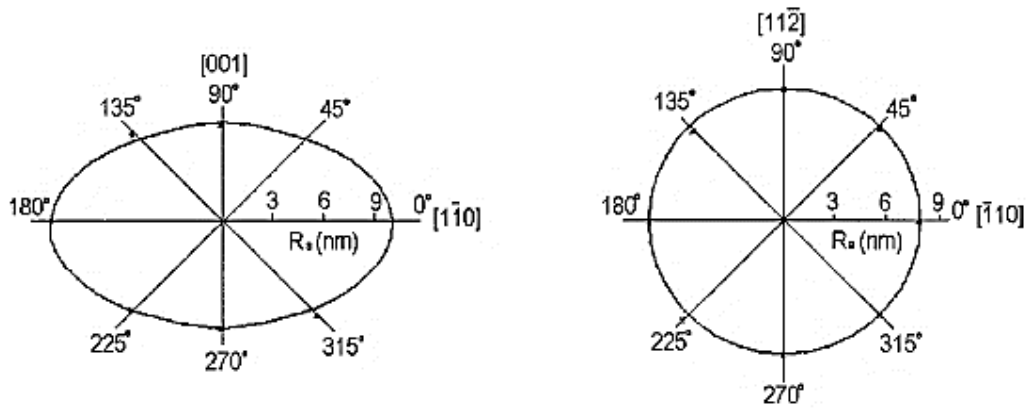


Figure 2-16 Variation of surface roughness with crystal orientation in diamond cutting of Cu single-crystals when cutting is performed on the (110) and the (111) plane, respectively [38]

Finally, by using a micro-plasticity Taylor model where the effective Taylor factor is used for determining the variation of the shear strength, they modelled the cutting force variation with crystallographic orientation as presented in the figure 2-17. They obtained a close match between the analytical predictions and experimental results.

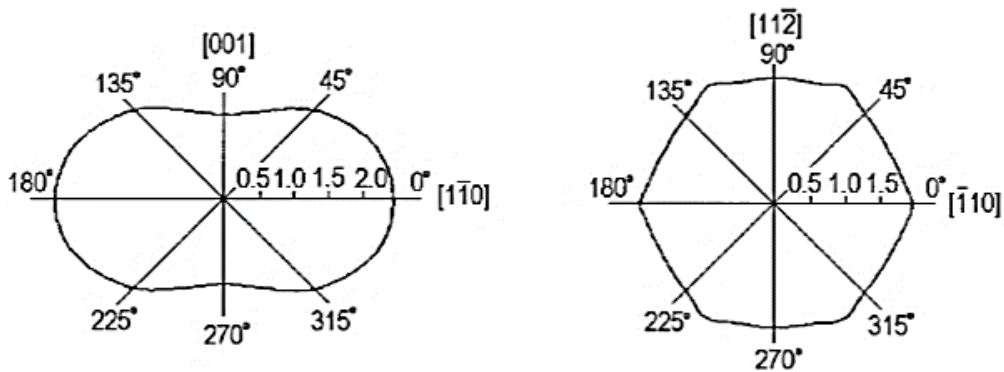


Figure 2-17 Variation of Taylor factor  $M'$  (shear strength) with crystal orientation when cutting when cutting is performed on the (110) and the (111) plane, respectively [38]

## 2.1 Strain Rate Effects

Modelling the responses of the materials at very high rates of deformation (which generally includes ranges  $>10^5 \text{ s}^{-1}$ ) has always been a challenging research area. Since the subject have many different application areas such as vehicular crash tests, development of armors, high

speed impact phenomena and also metal cutting, it is important to develop material models to give insight the nature of the deformation. It is well-known that material response during machining could be very complex; due to the involving high strain, strain rates and also temperature values. Austin et al. [2], develop a physically-based model to explain the slip mechanism in polycrystalline metals and alloys at very high strain rates (from  $10^4$  to  $10^8$   $s^{-1}$ ). Their model mainly focused on visco-plastic behavior of pure FCC metals in shock waves by using constitutive laws and the importance of this work arises from the treatment of the dislocation substructure and their approach to discuss the distinction between the mobile and immobile dislocation density. By taking account of this distinction and generating path-dependent formulations for the mobile and immobile dislocation density components, the weight or the effect of the dislocation population on the visco-plastic flow rate and the glide resistance can be evaluated. With this work, they changed the way of approaching the shock wave calculations where the rate-dependence is generally ignored.

Hansen et al. [14], developed a model where the deformation of single crystals for a wide-range of strain rates is formulated by using constitutive laws. In this work, they considered distribution of dislocation velocities to model plastic deformation and the model take account of both temperature and kinetic effects of dislocations moving at high rates, distinctively. Moreover, they obtain a good match with the experimentally observed transition between the two-different dislocation behavior.

It should be noted that even if the loading condition is at a certain strain rate, any point in microstructure could exhibit different behavior by enduring different strain rates due to the location of the point and the deformation history. There have been many different works which aim to model high strain rate behavior or from low to moderate strain rate values. Shahba and Ghosh [34], developed unified constitutive relations to adapt rate-dependent plasticity models to transcend a wide range of strain rates. In another way of saying, by developing a unified flow rule which considered the slip rate in terms of dislocation density and average dislocation velocity, they try to model the transcending from thermal-activated to drag-dominated stages. The results of CPFEE simulations based on their model are consistent with the experimental results for polycrystalline materials due to its ability to capture the increase in rate sensitivity of the flow stress at higher rates of deformation; and for single crystal materials, the model

predicts an elastic overshoot associated with the small amount of dislocation content at very high strain rate values.

## **2.2 Size-Effect**

Size-effect is another important consideration which again arises from the nature of the process. It is generally defined as the sudden non-linear increase in specific cutting energy. Since size-effect has been studied for the long time, many explanations are considered to give insight the mechanism. These explanations can be grouped as tool edge radius effect, sub-surface plastic deformation, material strengthening effect due to strain rate or strain gradient, and material separation effect.

Backer et. al [3] related the size effect to crystallographic defects and imperfections. They discussed that due to encountering significantly reduced number of imperfections when deformation takes place in a small volume, the material strength would be expected to increase.

In another explanation which is related with tool edge radius, the increase in specific cutting force with decrease in uncut chip thickness is explained by ploughing force arising from frictional rubbing and ploughing associated with material removal by a blunt tool. Moreover, any changes in tool edge radius can cause change in shear angle values and effective rake angle of the tool and this also can be considered as an explanation for the size-effect. In most of the studies, the main reason of the size effect is attributed to the relation between the edge radius of the tool and uncut chip thickness. Mian et al. [28] investigated the factors that dominate the size-effect in micro-machining. In order to explain the importance of the factors, they conducted micro-milling tests and they considered tool edge radius, cutting speed, chip load, and chip aspect ratio as the investigated factors. By using statistical analysis for the specific acoustic emission, they found that both ratio of feed per tooth to tool edge radius and the cutting velocity are the dominant factors which control the size-effect mechanism. Fang [11] developed a slip-line model for modelling the machining with a rounded edge tool. In his model, there are sub-regions which have their own physical meaning and the model to take into account of size effect, shear zone effect etc. Additionally, he proposed an equation to predict the thickness of the primary shear zone which also helps to predict the shear strain rate in the same zone.

According to the simulations of the model which considered orthogonal machining condition, tool edge radius is selected as the most important parameter affecting the process. Moreover, he found that since the nondimensionalized cutting force remains constant with increasing tool edge radius/uncut chip thickness ratio, it means that cutting force depends on the material shear flow and it leads to that the size effect highly depends on the material constitutive behavior in machining. It can be easily said that a good match is obtained between the classic-slip line theory and experimental evidence in zinc machining. Liu et al. [26] examined the effect of tool edge radius on the size-effect mechanism, by performing finite element simulations.

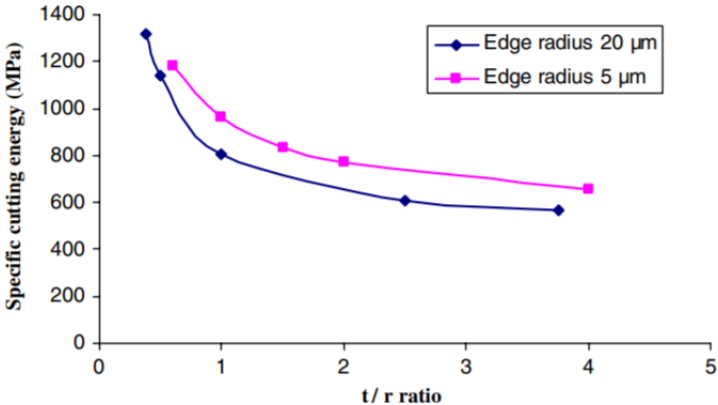


Figure 2-18 The variation of specific cutting energy with or ratio for two edge radii, without considering strain gradient effect [26]

They found that tool edge radius has an impact on the size-effect mechanism in two ways, first by changing the material flow pattern around the tool tip by widening the plastic shear zone and the second way because of higher energy dissipation due to increased tool-chip contact length at smaller uncut chip thickness values. It is evident from the figure 2-18 that the specific cutting energy increases when the t/r ratio decreases, which results in capturing the size effect in the simulations using a tool with edge radius.

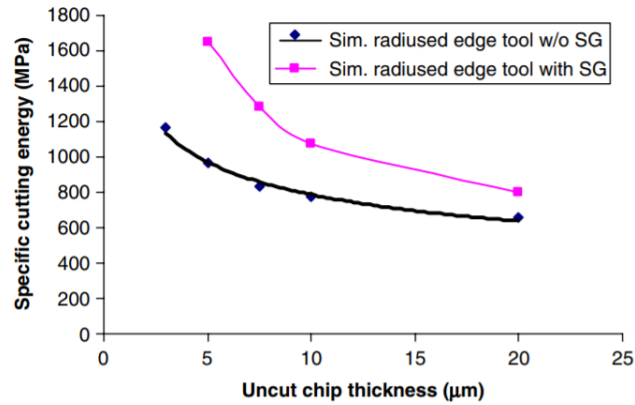


Figure 2-19 Variation of specific cutting energy with uncut chip thickness with and without strain gradient (SG) effect [26]

However, when the simulations are repeated by considering strain gradient effect, as can be seen in the figure 2-19 above, the results showed much greater increase in the specific cutting energy. As a result, they concluded that the tool edge radius can only be considered as a part of the reasons which causes the size-effect. In another way of saying, they proved that strain gradient strengthening of the material also causes size-effect mechanism when cutting at small uncut chip thickness levels. Another important finding is that at low cutting speeds, small uncut chip thickness and negligible tool radius values, nonlinear increase in specific cutting energy observed near the material length scale  $l$ . On the other hand, they also found that increasing the cutting speed also has an impact on the size effect because of the material strengthening in the secondary deformation zone.

Larsen-basse and Oxley [22] explained the size-effect occurrence in machining by considering strain-rate sensitivity of the workpiece material. According to the results of their experiments, on plain carbon steel, they concluded that the maximum shear strain rate within the primary shear zone is inversely proportional to the uncut chip thickness. Since a decrease in the uncut chip thickness causes an increase in the strain rate. This increase leads to an increase in the flow stress with the strain-rate sensitivity of flow stress increasing rapidly which can be considered as a reason for the increase in specific cutting energy with reduction in uncut chip thickness.

Kopalinsky and Oxley [18] explains the size-effect by considering the effect of temperature. They concluded that the size effect in machining at high cutting speeds and large uncut chip thickness is primarily caused by an increase in the shear strength of the workpiece material due to a decrease in the tool-chip interface temperature. They also emphasized that the effect of temperature is not the dominant mechanism at uncut chip thickness less than 50  $\mu\text{m}$ , which could be explained by increasing sensitivity of flow stress to strain rate within this range.

Finally, size-effect can be explained by considering the strain gradient plasticity theory. Due to the reduction in the shear plane length, an increase in the shear strain gradients and which leading to an increase in shear strength of the material is also considered as the reason of the size-effect. By using a strain gradient plasticity-based model of material deformation in the Primary Deformation Zone of an orthogonal cutting process and formulations of the strain gradient, density of geometrically necessary dislocations, shear strength of the material in the PDZ and the specific shear energy, the size-effect can be modeled in a more realistic way.

Joshi and Melkote [16] try to explain the size-effect mechanism in the PDZ by using strain gradient plasticity theory to model the plastic deformation in orthogonal machining process. Their model includes formulations to evaluate the strain gradient, density of geometrically necessary dislocations, shear strength of the material in PDZ and the specific shear energy. The schematic representation of the strain gradient model is given in the Figure 2-20 and 2-21 below.

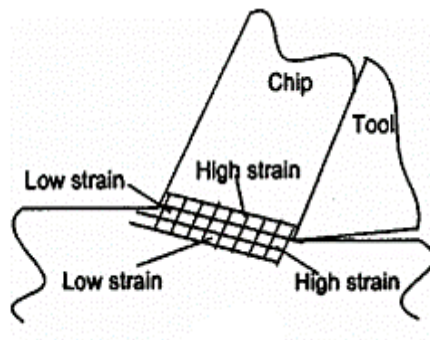


Figure 2-20 The schematic representation of the strain gradient model & overall PDZ [16]

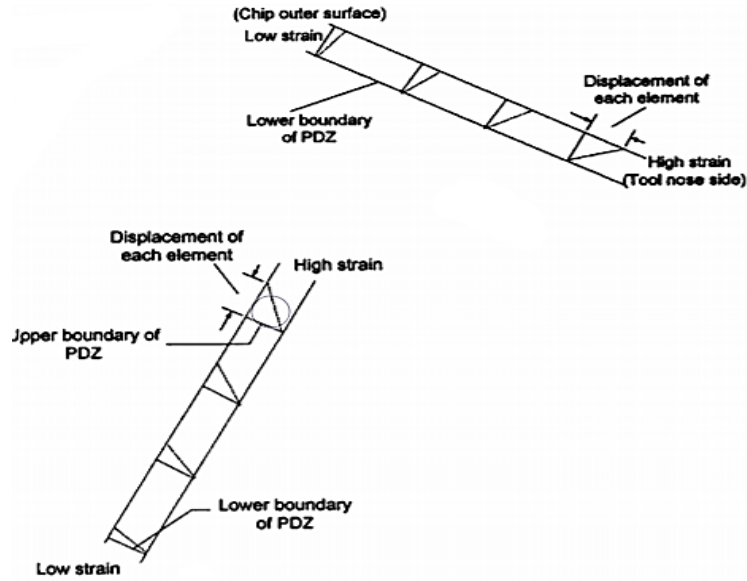


Figure 2-21 Model of strain gradient: in a row of elements parallel to the shear plane, in a row of elements perpendicular to the shear plane [16]

Moreover, they introduced a material length scale concept for modelling the deformation in PDZ. In this concept, the length of the shear plane was shown to be the material length scale governing the size-effect in PDZ. In another way of saying, as the length of the shear plane reduces, strain gradient increases leading to an increase in the shear strength. The increase in the shear strength of the material in the PDZ is considered as the lower bound on the size-effect in shear strength. By using their model, the amount of increase in shear strength can be evaluated.

The theoretical specific shear energy was obtained by using the equation (2.1) below,

$$u_{ss}^{model} = [1 + [\frac{\alpha^2 G b \sin \phi}{L \tau_0^2}]^\mu]^{1/2\mu} [\frac{\cos \alpha}{\cos(\phi - \alpha) \sin \phi}] \quad 2.1$$

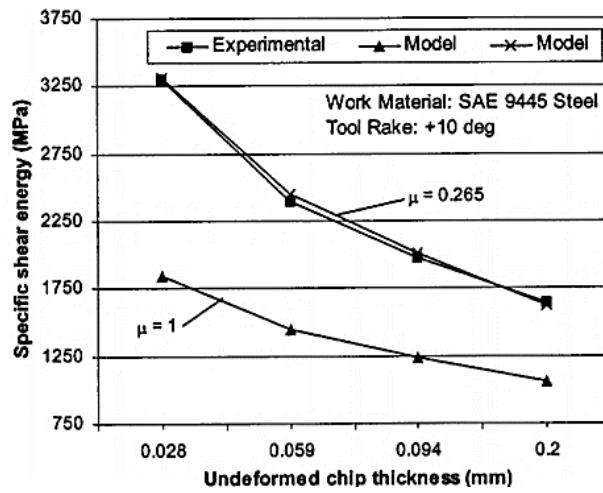


Figure 2-22 Size-effect in the specific shear energy- rake angle of the tool :10 deg[16]

In their work, they used three different experimental data sets to investigate the size-effect. The variation of specific shear energy with undeformed chip thickness evaluated from experimental data set and the one evaluated using their model is plotted in the figure 2-22 above. Since the maximum increase in shear strength is observed when the  $\mu=1$ , it is also depicted in the figure to show the lower bound on the size-effect. It can be said that their model predictions for specific shear energy has always the same trend with experimental values and a close match is also observed especially for  $\mu<1$ .

author / date	focus	machining type	material	machining parameters
Ueda and Iwata / 1980 [36]	experimental study & Schmid based model	orthogonal fly cutting	$\beta$ -brass single crystals	rake angle: $0^\circ / 20^\circ$ depth of cut: 10-30 $\mu\text{m}$ width of cut: 1 mm edge radius 774 $\mu\text{m}$ cutting speed: 0.15 mm/min
Cohen, P. / 1982 [6]	experimental study	micro turning	Al and Cu single crystals	rake angle: $20^\circ / 40^\circ / 50^\circ$ depth of cut: 114.3 $\mu\text{m}$ width of cut: 15-20 $\mu\text{m}$ edge radius: 2 $\mu\text{m}$ cutting speed: 0.55 mm/s
Kopalinsky et al. / 1984 [18]	experimental Study	orthogonal machining	Plain Carbon Steel	rake angle: $-5^\circ / -25^\circ / -50^\circ$ depth of cut: 2mm width of cut: - edge radius: Negligible cutting speed: 420 m/min
Blackley and Scattergood / 1990 [4]	experimental study & stress based model	facing	Ge single crystals	rake angle: $0^\circ / -10^\circ / -30^\circ$ depth of cut: 5/ 2.5 $\mu\text{m}$ /0.5 $\mu\text{m}$ width of cut: - edge radius: 0.762 /3.175 mm cutting speed: 1 m/s
Sato et al. / 1991 [33]	experimental study	orthogonal cutting with milling	Al single crystal	rake angle: $3^\circ$ depth of cut: 0.5-3 $\mu\text{m}$ width of cut: 4.5 mm nose radius 10 mm cutting speed: 1 m/min
Lee and Zhou / 1993 [24]	Taylor based microplasticity model	orthogonal fly cutting	$\beta$ -brass single crystals	Ueda and Iwata experiments
Moriwaki / 1993 [29]	experimental study	orthogonal fly cutting and quasi-orthogonal cutting	Cu single crystals	rake angle: $0^\circ$ depth of cut: 0.01 -3 $\mu\text{m}$ width of cut: - edge radius: Negligible cutting speed: 530m/min
To et al. /1997 [35]	experimental study	Diamond Turning	Al single crystals	rake angle 0 deg. depth of cut 1-10 $\mu\text{m}$ edge radius 0,635 mm cutting speed 319000 mm/min
Zhou and Ngoi / 2001 [38]	experimental study & Taylor based model	Diamond Turning	Al and Cu single crystals	rake angle: $0^\circ$ depth of cut: 5 $\mu\text{m}$ width of cut: - edge radius 500 $\mu\text{m}$ cutting speed: 78 m/min
Lee et al. / 2002 [25]	experimental study & Taylor based model	facing	Al single crystals	rake angle: $0^\circ$ depth of cut: 0.1-200 $\mu\text{m}$ width of cut: 4 mm edge radius: - cutting speed: 78000 mm/min
Kota and Ozdoganlar / 2010 [19]	Taylor based model	planing	Al and Cu single crystals	Cohen experiments
Demiral et al. / 2014 [10]	crystal plasticity finite element model	planing	Al and Cu single crystals	rake angle: $0^\circ$ depth of cut: 2 $\mu\text{m}$ width of cut: 1.6 $\mu\text{m}$ edge radius: - cutting speed: 1300 mm/s

Table 2-1 Summary of single crystal micro machining works

### 3 MACHINING PLASTICITY MODEL

The material model includes three main parts: in the first part, mechanics of the orthogonal machining process and related force and velocity expressions are discussed. In the 2<sup>nd</sup> part, single crystal deformation kinematics formulations are given. Finally, the last part includes related single crystal constitutive laws.

#### 3.1 Orthogonal Machining Mechanics

Orthogonal machining has the simplest geometry in all machining operations and the real-life application for this process mechanics could be planning or turning. For that reason, it could be used as a base for explaining general mechanics of the material removal and more complex process geometries such as milling, drilling. It can be defined as a cutting process in which cutting edge of a straight tool is perpendicular to the cutting velocity. In the proposed model, there are two assumptions related with orthogonal cutting which are plane strain and sharp tool assumptions. Since the material deformation is considered as uniform along the cutting edge, it can be assumed that the orthogonal cutting is a two-dimensional plane strain deformation process. Moreover, the tool is considered as sharp as possible due to avoiding tool edge radius effects such as size-effect. In the fig.1 below, the schematic representation of orthogonal machining geometry, shear plane and chip formation is given.

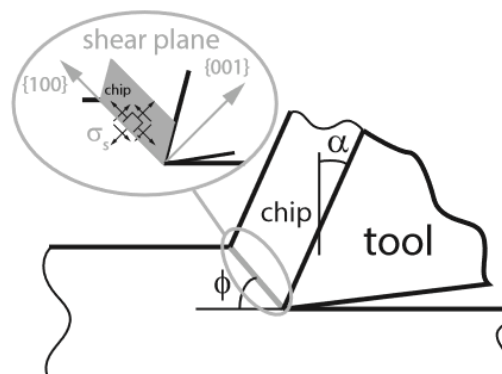


Figure 3-1: The schematic representation of orthogonal machining, tool and chip formation

Since the tool is considered as sharp as possible, the depth of cut value is assumed to be greater than the edge radius of the tool and the deformation geometry of orthogonal cutting is assumed to be simple shear on the shear plane. In this model, friction between the chip and the rake face also considered while the friction or any rubbing effect between the workpiece material and the flank face of the cutting tool is neglected. There are three main zones should be considered during modelling the orthogonal machining process. Primary zone is the region which includes shear plane and it is presented by details in the figure 3-1 above. While the tool penetrates the workpiece, the material advances toward the tool and it is sheared over the primary shear zone to form a chip. Secondary deformation zone includes the region between the chip and the rake face of the tool. The last region where the flank of the tool rubs the newly machined surface, is called the tertiary zone. The effect of the tertiary deformation zone is neglected in this study.

There are different approaches to model the primary deformation zone but two of them could be considered as the most accepted the approaches. The model that the Merchant developed used the assumption of thin plane for the shear zone whereas the others based on thick shear deformation zone. As it is mentioned before, thin shear zone assumption is used in this study for simplification. The deformation geometry and the cutting forces are shown on the cross-sectional view of the orthogonal machining is presented in figure 3-2 below;

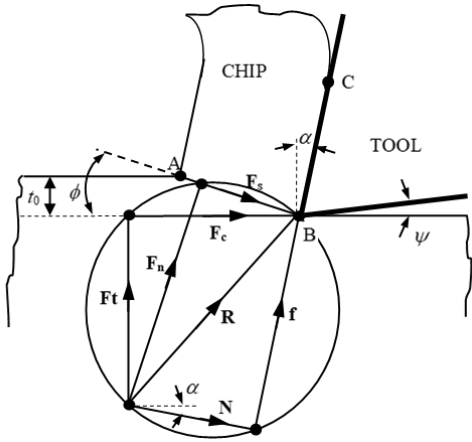


Figure 3-2 : The cross-sectional view of the orthogonal machining and cutting forces

In orthogonal cutting, cutting forces are exerted only in the directions of velocity and uncut chip thickness, which are called tangential ( $F_t$ ) and feed forces ( $F_c$ ), and it is different from oblique cutting in which the cutting edge is oriented with an inclination angle ( $i$ ) and the

additional third force acts in the radial direction ( $F_r$ ). It should be noted that cutting forces action on the tool will have equal amplitude but opposite direction compared to the forces acting on the chip. The R notation is used for resultant force and f and  $F_s$  imply the friction and shear forces, respectively [1]

$$f = \frac{\sin \beta}{\cos(\phi + \beta - \alpha)} F_s \quad 3.1$$

$$R = \frac{F_s}{\cos(\phi + \beta - \alpha)} \quad 3.2$$

$$F_c = R \cos(\beta - \alpha) \quad 3.3$$

$$F_t = R \sin(\beta - \alpha) \quad 3.4$$

In order to obtain the shear and friction power formulations,  $\dot{W}_f$  and  $\dot{W}_s$  same expressions can also be derived for V,  $V_c$  and  $V_s$  refer to cutting velocity, chip velocity and shear velocity, respectively.

$$\frac{V_c}{\sin \phi} = \frac{V}{\cos(\phi - \alpha)} = \frac{V_s}{\cos \alpha} \quad 3.5$$

$$\dot{W}_f = fV_c \quad 3.6$$

$$\dot{W}_s = F_s V_s = \frac{\cos(\alpha)}{\cos(\phi - \alpha)} F_s V \quad 3.7$$

In order to determine the total power, sum of the shear power and friction power is calculated:

$$\dot{W}_{tot} = \dot{W}_f + \dot{W}_s = \frac{\sin \beta \sin \phi}{\cos(\phi + \beta - \alpha) \cos(\phi - \alpha)} + \frac{\cos \alpha}{\cos(\phi - \alpha)} F_s V \quad 3.8$$

The total amount of shear,  $\gamma$ , as a function of shear angle,  $\phi$ , and rake angle,  $\alpha$ , is presented in the equation below,

$$\gamma = \cot \phi + \tan(\phi - \alpha) = \frac{\cos \alpha}{\sin \phi \cos(\phi - \alpha)} \quad 3.9$$

Specific cutting energy,  $K_c$ , energy required to remove a unit volume of material and it is generally expressed as a function of workpiece material, tool and process:

$$K_c = \frac{C.Power}{MRR} = \frac{F_c}{wt_0} = \frac{\cos(\beta - \alpha)}{\cos(\phi + \beta - \alpha)} \frac{F_s}{wt_0} \quad 3.10$$

The total amount of time for shearing process,  $t$  is calculated by dividing the distance travelled during shear,  $L$ , by the shear velocity,  $V_s$ .

$$L = \frac{t_0}{\sin \phi} \quad 3.11$$

$$t = \frac{L}{V_s} \quad 3.12$$

The total work,  $W_{tot}$ , could be calculated by adding the power increments over time.

$$W_{tot} = \int \dot{W}_{tot} dt \quad 3.13$$

### 3.2 Crystal Orientation and Deformation Geometry

As mentioned before, since the material deformation is considered as uniform along the cutting edge, orthogonal cutting can be considered as a two-dimensional plane strain deformation process. In the case of plane strain the total deformation gradient,  $F$ , is defined as in the form of simple shear on the shear reference frame:

$$\mathbf{F} = \begin{pmatrix} 1 & 0 & \gamma \\ 0 & 1 & 0 \\ 0 & 0 & 1 \end{pmatrix} \quad 3.14$$

Then, the transformation between the shear reference frame and the crystal reference frame should be determined. Shear, cutting and the crystal reference frames are presented in the figure 3-3 below,

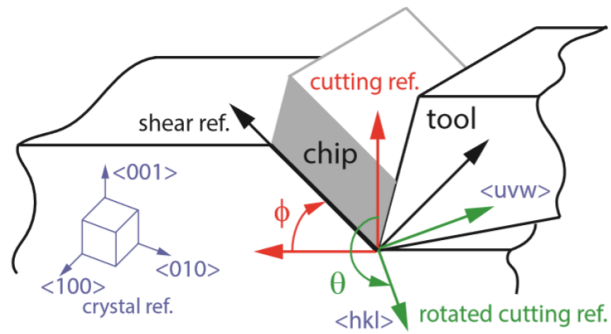


Figure 3-3 Shear reference (in black color), cutting reference (in red color), rotated-cutting reference (in green color) and crystal reference (in blue color) with  $\theta$ : rotation angle about the zone axis,  $\varphi$ : shear angle

In the first step, transformation matrix ( $\mathbf{T}_{c \rightarrow sh}$ ) from shear reference frame to the cutting reference frame prescribed by the rotation of the shear angle ( $\varphi$ ). The axis of rotation coincides with the width direction of the cut sample. The shear angle has a negative sign by definition.

$$\mathbf{T}_{c \rightarrow sh} = \begin{bmatrix} \cos \phi & 0 & -\sin \phi \\ 0 & 1 & 0 \\ \sin \phi & 0 & \cos \phi \end{bmatrix} \quad 3.15$$

Then, transformation matrix from the rotated cutting reference to the cutting reference frame ( $\mathbf{T}_{rc \rightarrow c}$ ) is computed. Since the crystal rotates with respect to the tool during the turning process,

a rotation angle,  $\theta$  is defined about the zone axis vector  $\{pqr\}$  which is normal to both the cutting direction and the cutting plane.

$$\mathbf{T}_{rc \rightarrow c} = \begin{bmatrix} \cos \theta & 0 & \sin \theta \\ 0 & 1 & 0 \\ -\sin \theta & 0 & \cos \theta \end{bmatrix} \quad 3.16$$

Finally, transformation matrix from the rotated-cutting reference frame to the crystal frame ( $\mathbf{T}_{rc \rightarrow cr}$ ) is computed. It is constructed using crystallographic vectors of  $\{uvw\}$ ,  $\{pqr\}$ , and  $\{hkl\}$ , respectively, corresponding to the first, second, and third directions of the rotated-cutting reference.

$$\mathbf{T}_{rc \rightarrow cr} = \begin{bmatrix} u & p & h \\ v & q & k \\ w & r & l \end{bmatrix} \quad 3.17$$

Therefore, the overall transformation matrix,  $\mathbf{R}$ , from the shear reference frame to the crystal reference frame can be defined as,

$$\mathbf{R} = \mathbf{T}_{rc \rightarrow cr} \mathbf{T}_{rc \rightarrow c} \mathbf{T}_{c \rightarrow sh} \quad 3.18$$

### 3.3 Single Crystal Deformation Kinematics

Since the chip formation in metal cutting is associated with large strains and high strain rates, a large deformation crystal plasticity framework is adopted in this study. Deformation gradient,  $\mathbf{F}$ , is the measure of the total change in shape and it is specified as shearing,  $\gamma$ , on the shear plane. It can be expressed as in matrix form given in equation below:

$$\mathbf{F} = \begin{pmatrix} 1 & 0 & \gamma \\ 0 & 1 & 0 \\ 0 & 0 & 1 \end{pmatrix} \quad 3.19$$

Total amount of deformation gradient consists of elastic and plastic parts [16].

$$\mathbf{F} = \mathbf{F}^e \mathbf{F}^p \quad 3.20$$

Elastic strains which is the form of strain in which the distorted body returns to its original shape and size when the deforming force is removed can be computed by using Green-Lagrange strain tensor.

$$\mathbf{E}^e = \frac{\mathbf{F}^{eT} \mathbf{F}^e - \mathbf{I}}{2} \quad 3.21$$

Then, the vectorized form of stresses,  $\hat{\mathbf{p}}$  can be calculated by using vectorized form of Green-Lagrange strain,  $\mathbf{e}^e$  and the cubic elasticity tensor,  $\hat{\mathbf{C}}$  at the crystal reference frame.

$$\hat{\mathbf{p}} = \hat{\mathbf{C}} \cdot \mathbf{e}^e \quad 3.22$$

$\mathbf{C}$  implies the elasticity matrix in the crystal frame constructed using three temperature dependent elastic constants for cubic metals;  $C_{11}$ ,  $C_{12}$ , and  $C_{44}$  for aluminum.

$$C_{11} = 123.323 + 6.7008 \times 10^{-8} T^3 - 1.1342 \times 10^{-4} T^2 - 7.8788 \times 10^{-3} T \quad 3.23$$

$$C_{12} = 70.6512 + 4.4105 \times 10^{-8} T^3 - 7.5498 \times 10^{-5} T^2 + 3.9992 \times 10^{-3} T \quad 3.24$$

$$C_{44} = 123.323 + 7.0477 \times 10^{-9} T^3 - 1.2136 \times 10^{-5} T^2 - 8.3274 \times 10^{-3} T \quad 3.25$$

$$\mathbf{C} = \begin{pmatrix} C_{11} & C_{12} & C_{12} & 0 & 0 & 0 \\ C_{12} & C_{11} & C_{12} & 0 & 0 & 0 \\ C_{12} & C_{12} & C_{11} & 0 & 0 & 0 \\ 0 & 0 & 0 & C_{44} & 0 & 0 \\ 0 & 0 & 0 & 0 & C_{44} & 0 \\ 0 & 0 & 0 & 0 & 0 & C_{44} \end{pmatrix} \quad 3.26$$

The resolved shear stress,  $\tau^a$ , per slip system, a, is determined by resolving 2<sup>nd</sup> Piola Kirchoff stress.

$$\tau^a = \mathbf{F}^{eT} \mathbf{F}^e \hat{\mathbf{P}} : \hat{\mathbf{S}}^a \quad 3.27$$

Where  $\hat{\mathbf{S}}^a$  is the Schmid tensor which is defined as the dyadic product of slip direction,  $\hat{\mathbf{s}}^a$ , and slip plane normal,  $\hat{\mathbf{n}}^a$ , for slip system a.

$$\hat{\mathbf{S}}^a = \hat{\mathbf{s}}^a \otimes \hat{\mathbf{n}}^a \quad 3.28$$

In the table-1 below, the slip plane normal and the slip direction of the FCC-type crystal systems in the crystal reference frame is presented.

Table 1 :	Slip System for F.C.C. Crystals ; $\bar{s}^a$ and $\bar{n}^a$ denote slip direction and slip plane normal, respectively											
$\bar{n}^a$	(111)			$(\bar{1}\bar{1}\bar{1})$			$(\bar{1}11)$			$(1\bar{1}\bar{1})$		
$\bar{s}^a$	$[\bar{0}1\bar{1}]$	$[\bar{1}0\bar{1}]$	$[\bar{1}\bar{1}0]$	$[\bar{0}\bar{1}\bar{1}]$	$[\bar{1}01]$	$[\bar{1}\bar{1}0]$	$[01\bar{1}]$	$[101]$	$[\bar{1}\bar{1}0]$	$[0\bar{1}\bar{1}]$	$[\bar{1}0\bar{1}]$	$[110]$

Table 3-1: Slip system for FCC crystals;  $\bar{s}^a$  and  $\bar{n}^a$  denote the slip direction and slip plane normal, respectively, in the crystal reference frame

The rate of the plastic part of the deformation gradient is calculated in terms of the velocity gradient,

$$\dot{\mathbf{F}}^p = \mathbf{L}^p \mathbf{F}^p \quad 3.29$$

To calculate the plastic velocity gradient,  $\mathbf{L}^p$ , the shear rates over the slip systems are summed up.

$$\mathbf{L}^p = \sum_{\alpha=1}^{12} \hat{\mathbf{S}}^{\alpha} \dot{\gamma} \quad 3.30$$

The stress at the deformed reference, i.e., the Cauchy stress,  $\boldsymbol{\sigma}$ , is calculated using the equation below,

$$\boldsymbol{\sigma} = \frac{\mathbf{F}^e \hat{\mathbf{P}} \mathbf{F}^{eT}}{\det(\mathbf{F}^e)} \quad 3.31$$

Crystal plasticity kinematic equations are solved using the Dawson-Maniatty algorithm [27]. The novelty of this study from the previous studies is the usage of the zero-penalty parameter ( $\lambda_p = 0$ ) which helps to enforce volume constancy. Since it is well-known that in case of machining, chip formation is associated with large strain and high strain rates; therefore, the amount of simple shear for machining can take very large values (well over ( $^{\circ}90$ )) especially for low shear angles ( $\phi$ ). To obtain healthier results, the volume constancy enforcement and the related penalty term are neglected in this study.

### 3.4 Physics-Based Single Crystal Constitutive Model

In order to find the slip rates,  $\dot{\gamma}^a$  and the resolved shear stress,  $\tau^a$ , different plastic constitutive laws are used. All constitutive laws used in this study, presented in the table below.

#### 3.4.1 Dislocation Geometry

In the aspect of FCC crystals, the dominant dislocation mechanism is assumed as edge-type. Forest dislocations are defined as the dislocations that intersect the plane and they can be considered as obstacles to the motion of the gliding dislocation that, to a reasonable approximation, can be treated as point obstacles in the glide plane.



Figure 3-4 TEM images of a deformed single crystal [21]

Figure 3-4 shows the TEM measurements that this work relies on. The dislocation dense regions consist of mainly edge type dislocations. In the TEM image the dense regions are along normal direction the glide direction which verifies that they are of edge type. According to Kocks [17] and Kuhlmann [21], the interior regions consisted of screw type of mobile dislocations.

### 3.4.1.1 Forest Dislocation Density

Forest dislocations are the type of dislocations which intersects or piercing through the slip plane. By using the assumption of edge type dislocation geometry for the primary dislocations, which is consistent with etch-pit observations, the forest dislocation density on the slip system  $\alpha$  can be calculated with the projection of the directions of the primary edge type dislocations with line direction,  $t^z$ , onto the other slip plane normal,  $n^a$ .

$$\rho_f^a = \sum_{z=1}^{12} x_z^a |t^z n^a| \rho^z \quad 3.32$$

where  $x_z^a$  is the dislocation interaction matrix that accounts for the difference in the forest interactions among the slip systems [12]. Moreover, they refer to the self, co-planar, cross-slip, glissile, Hirth lock, and Lomer-Cottrell lock dislocation interactions, respectively.

$$x_z^\alpha = \begin{bmatrix} i_0 & i_1 & i_1 & i_4 & i_5 & i_3 & i_4 & i_3 & i_5 & i_2 & i_3 & i_3 \\ & i_0 & i_1 & i_5 & i_4 & i_3 & i_3 & i_2 & i_3 & i_3 & i_4 & i_5 \\ & & i_0 & i_3 & i_3 & i_2 & i_5 & i_3 & i_4 & i_3 & i_5 & i_4 \\ & & & i_0 & i_1 & i_1 & i_2 & i_3 & i_3 & i_4 & i_3 & i_5 \\ & & & & i_0 & i_1 & i_3 & i_4 & i_5 & i_3 & i_2 & i_3 \\ & & & & & i_0 & i_3 & i_5 & i_4 & i_5 & i_3 & i_4 \\ & & & & & & i_0 & i_1 & i_1 & i_4 & i_5 & i_3 \\ & & & & & & & i_0 & i_1 & i_5 & i_4 & i_3 \\ & & & & & & & & i_0 & i_3 & i_3 & i_2 \\ & & & & & & & & & i_0 & i_1 & i_1 \\ & & & & & & & & & & i_0 & i_1 \\ & & & & & & & & & & & i_0 \end{bmatrix} \quad 3.33$$

The line directions of edge-type dislocations,  $\mathbf{t}^\beta$  can be expressed as follows :

$$\mathbf{t}^z = \mathbf{s}^z \times \mathbf{n}^z \quad 3.34$$

where the  $\mathbf{s}^z$  and  $\mathbf{n}^z$  imply the slip direction and the slip plane normal, respectively. Figure 3-5 shows the forest dislocation projection of an edge type of dislocation in slip system z onto slip system a.

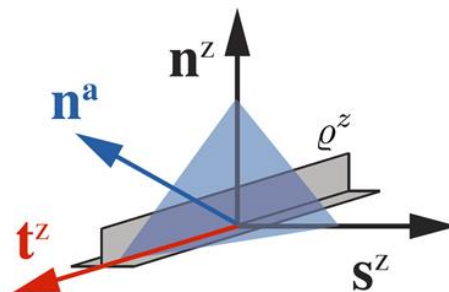


Figure 3-5 The schematic representation of the forest dislocation projection of an edge type of dislocation in slip system z onto slip system a.

### 3.4.1.2 Forest Spacing

Forest dislocations which intersect the plane can be considered as obstacle to the motion of the gliding dislocation. If the density of the forest dislocations which are arranged on a simple cubic network, is assumed as  $\rho_f$ , then  $\rho_f^{(1/2)}$  is the number of the dislocations per unit length, and as a result,  $\rho_f^{-(1/2)}$  gives the dislocation spacing.

$$d^a = \frac{c_1}{\sqrt{\rho_f^a}} \quad 3.35$$

Furthermore, the similarity rule suggests that  $d$  remains proportional to  $D$  which is the distance between the dislocation dense regions is referred to as the mean free path.

### 3.4.2 Dislocation Kinetics

In the preceding chapter, the motion of individual dislocations will be described and the information on dislocation kinetics will be presented.

#### 3.4.2.1 Slip Rate

Shear rate could be determined by using the Orowan's equation where the plastic shearing is considered as a result of expanding dislocation loops that glides with average slip velocity  $v^a$  presented below.

$$\dot{\gamma}^a = \rho_m^a b v^a \text{sgn}(\tau^a) \quad 3.36$$

where  $\rho_m$  is the density of mobile dislocations from the active slip set,  $v^a$  is the average dislocation velocity multiplied by Burger's vector and sign function of the resolved shear stress of the corresponding slip plane. Orowan's equation helps to set the relationship between the average shear rate and the movement of mobile dislocations on each slip system. It is difficult

to predict strain-hardening behavior of the material because strain depends on the both  $\rho$  and dislocation distribution.

### 3.4.2.2 Mobile Dislocation Density

In order to formulate the evolution laws for dislocation densities, the rate equations which includes production and annihilation terms are used. Dislocation density of the immobile dislocations can be easily formulated by using this approach; however, for the mobile dislocation densities there is no such simple model to define its evolution. The unpredictability associated with the number of mobile dislocations and their average slip velocity effect on the plastic deformation rate makes the mobile dislocation density is the most unknown and least measurable quantity.

Therefore, assuming a log-normal distribution for the segment lengths can be a reasonable way to calculate the mobile dislocation density as a function of the state variables (stress and dislocation density). Then, by taking the integral of the fraction of mobile dislocation segments,  $r(\tau, \Lambda_0)$  through the segment length, mobile dislocation density equation obtained. In this aspect, the segment lengths that are longer than the critical segment length are considered as mobile. Figure 3-7 shows the schematic representation of the dislocation segments and simplified and the log-normal for a mean segment length of  $10^{-6}$  m.

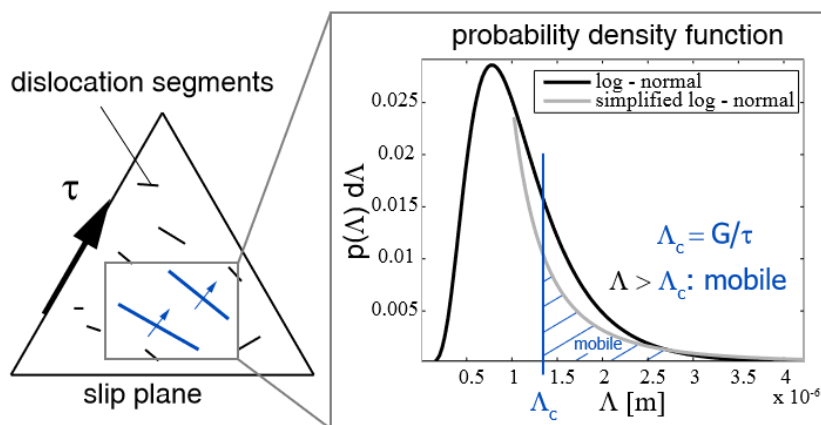


Figure 3-6  $\Lambda$  versus  $p(\Lambda) d\Lambda$ , the simplified and the log-normal probability density function for a mean segment length,  $\Lambda_0$ , of  $10^{-6}$  m.

$$\rho_m^\alpha = (2\pi)^{\frac{3}{2}} \left(\frac{\tau^\alpha}{Gb}\right)^2 \frac{1}{\rho_f^\alpha} \rho^\alpha \quad 3.37$$

The mobile dislocation density equation becomes as in equation (3.37) above, in terms of Burger's vector ( $b$ ), shear modulus ( $G$ ), the resolved shear stress per slip system ( $\tau^\alpha$ ), the forest dislocation density ( $\rho_f^\alpha$ ) and the primary dislocation density ( $\rho^\alpha$ ).

### 3.4.2.1 Long-Range Stress (Athermal Stress)

The flow stress has both short and long-range components. The excess storage of the edge-type dislocations of one sign inside the dislocation dense regions causes athermal stress. Figure 3-7 shows the internal stress fields encountered by dislocation through the crystal lattice.

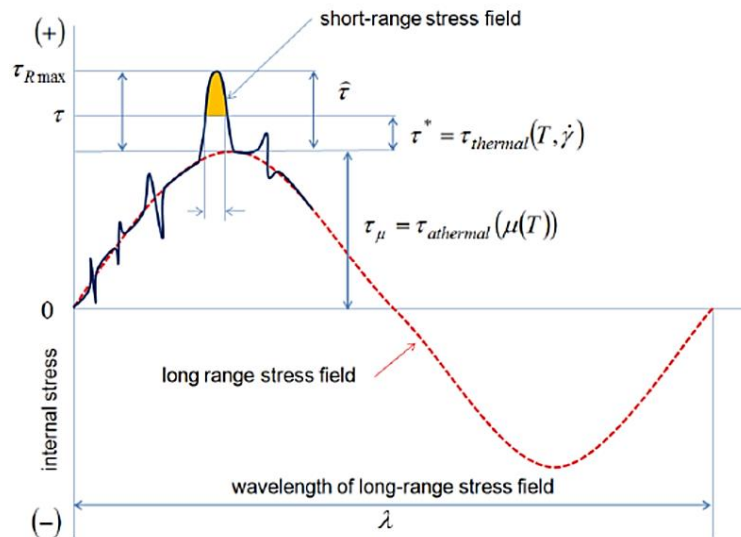


Figure 3-7 Schematic drawing showing internal stress fields during dislocation movement through the crystal lattice [7]

The long-range athermal part of the stress can be determined by using the Taylor relation from the density of the primary dislocations which are assumed to have an edge-type dislocation geometry. Therefore, it can be computed by using the equation as follows:

$$\tau_{\mu}^{\alpha} = c_2 G b \sqrt{\rho^{\alpha}}$$

3.38

where  $\rho^{\alpha}$ ,  $c_2$ ,  $G$  and  $b$  implies the density of primary dislocations of the slip system  $\alpha$ , geometric factor, and shear modulus, and Burger's vector, respectively.

### 3.4.2.2 Thermally-Activated Glide Velocity

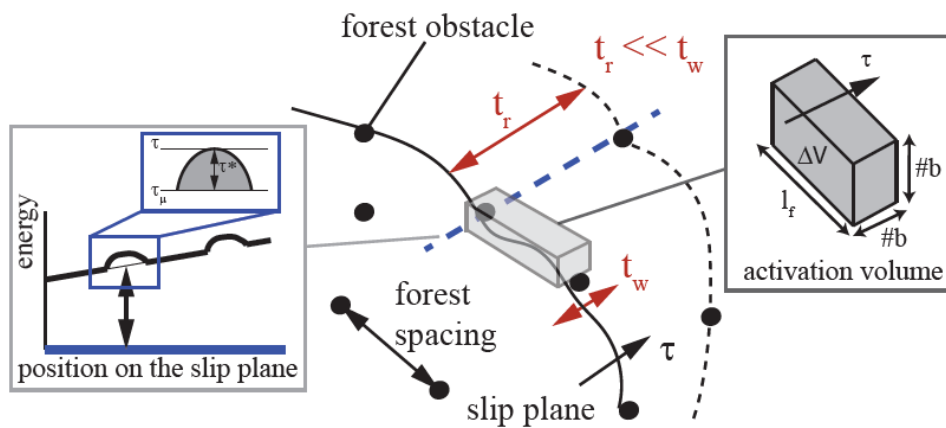


Figure 3-8 Schematic sketch of the thermally activated glide process

Glide of the dislocations can be defined as the movement of a dislocation on its slip plane. Dislocation glide allows plastic deformation to occur at a much lower stress than would be required to move a whole plane of atoms past another. Figure 3-8 visualizes the mechanism of the thermally activated glide process.

It is assumed that the dislocations move in a periodic potential and since the single crystal structure consists of obstacles, gliding dislocation encounters an obstacle after travelling a distance  $d$ . Therefore, by using the waiting time of the dislocation segment in front of obstacles,  $t_w$ , until achieving sufficient energy temperature  $T$  to move past an obstacle, average glide velocity,  $v$  can be obtained.

$$v^a = \frac{d^a}{t_w} \quad 3.39$$

where  $d$  implies obstacle-free distance travelled by a dislocation and it is proportional to the forest dislocation spacing.

The waiting time of the dislocation segment in front of obstacles,  $t_w$ , could be written in terms of frequency factor,  $v_g$  and Boltzmann factor,  $K$ , temperature,  $T$  and the activation free energy,  $\Delta G$ , that needs to be supplied by the thermal fluctuations in the crystal lattice.

$$t_w = v_g \exp\left(\frac{\Delta G}{KT}\right) \quad 3.40$$

The required activation free energy,  $\Delta G$ , could be written in terms of Helmholtz free energy associated with the thermal activation process,  $\Delta F$ , activation volume,  $V$ , and the short-range component of the flow stress,  $\tau$ .

$$\Delta G = \Delta F - \tau * v \quad 3.41$$

The flow stress,  $\tau$ , has separated into two components which are temperature-independent long range,  $\tau_\mu$  and strongly temperature-dependent short-range components,  $\tau^*$ . The thermal part of the flow stress arises from the short-range retarding force between the forest dislocations and the gliding dislocations whereas the long-range component arises due to having excess storage of edge-type dislocations of one sign inside the dislocation-dense regions.

$$|\tau| = \tau^* + \tau_\mu \quad 3.42$$

The athermal part of the flow stress,  $\tau_\mu$ , can be computed by using the equation(3.39) which already given above.

Activation volume can be written in terms of terms of  $l$  and  $\Delta R$ , the average length of dislocation at each obstacle and activation distance, respectively.

$$V = b l \Delta R \quad 3.43$$

Since the length of dislocation in front of an obstacle,  $l$  is assumed to have the same magnitude as the forest dislocation spacing, and  $c_3$  refers to the adjusting parameter for the jump distance associated with a thermal activation event, the equation 3.44 becomes,

$$V^a = \frac{c_3 b^2}{\sqrt{\rho_f^a}} \quad 3.44$$

The expression for average glide velocity takes the final form as follows:

$$v^a = v_g d^a \exp\left(-\frac{\Delta F}{KT}\right) \exp\left(\frac{|\tau^a| - \tau_\mu^a}{KT} V^a\right) \quad 3.45$$

### 3.4.2.3 Dislocation Drag Velocity

It is known that dislocation motion through an array of obstacles in metals includes coupling of thermally activated and drag-dependent processes. In two different regions, two different dislocation behaviors are observed. In low-velocity region which is considered as between ( $10^{-6}$ - $1$  m/s), the behavior is non-linear and velocity is considered as obstacle dominated. However, in the second region (above about 1 m/s) where the motion is drag dependent, velocity is linear and there is no strong effect of obstacle observed on the dislocation behavior.

Then the interaction of a moving dislocation with phonons or electrons can limit its velocity and the strength of the interaction is measured by the *drag coefficient*,  $B_0$ .

$$V_{dr}^a = \frac{b(\tau^a - \tau_\mu^a)}{B_0} \quad 3.46$$

where  $b$  and  $\tau^a - \tau_\mu^a$  is the Burger's vector and effective stress, respectively. The effective stress does not have long-range component or in another way of saying, effective stress only takes account of pushing dislocation over the short-range obstacles.

### 3.4.2.4 Unified Flow Rule

Since the material behavior changes with the strain rate, the dislocation kinetics model should also change with different strain rate values. It is known that, at low strain rates deformation is controlled by thermally activated glide. On the other hand, when the strain rate values achieve relatively high values (above  $10^4 \text{ s}^{-1}$ ), the dominant mechanism for crystallographic shearing becomes the viscous drag.

To combine two average velocities, the unified flow rule is used which equals to the geometric average of the two relations:

$$\frac{1}{v^\alpha} = \frac{1}{v_{dr}^\alpha} + \frac{1}{v_{th}^\alpha} \quad 3.47$$

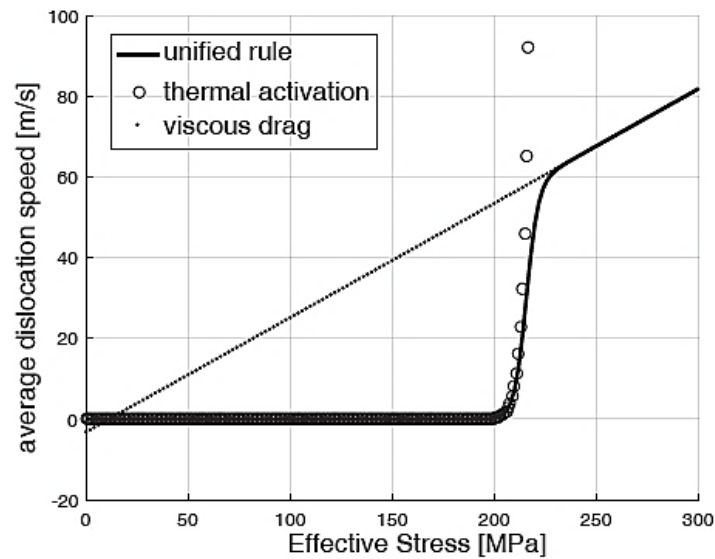


Figure 3-9 Effective stress (MPa) vs. average dislocation velocity (m/s) for thermally-activated glide, viscous drag, and unified rule.

By implementing the unified approach in this work, the model can be used for a wide range of strain rates. Moreover, it also helps to obtain a numerically stable solution for the dislocation velocity. Figure 3-9 shows the relation between the effective stress and the average dislocation

velocity (m/s) for thermally-activated glide, viscous drag, and unified rule. The combination of two mechanism allows smooth transition of plastic deformation depending on the strain rate. As a result, this approach presented in the earlier works makes the dominant dislocation kinetics as thermally activated glide at low strain rates and viscous drag at high strain rates.

### 3.4.3 Dislocation Density Evolution

To explain the strain hardening behavior of the materials, it is required to define properly and combine the relation between the storage of the dislocations and dynamic recovery mechanism behavior during plastic deformation. In order to take account of effect of dislocation geometry on the mechanical behavior of FCC crystals, it is important to understand mechanisms between the dislocation interactions. The main reason of this assumption is the annihilation of the screw dislocation dipoles due to the cross-slip mechanism. If the two dislocations of opposite sign and having the same plane attract each other, dislocation annihilation occur when they meet. Figure 3-10 explains the annihilation mechanisms in dislocation interactions.

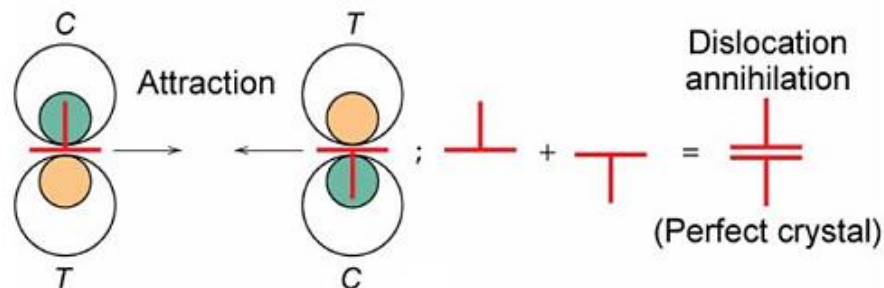


Figure 3-10 The schematic representation of the dislocation annihilation [5]

The screw dislocations move in (111) plane but they can switch to another plane if it contains the direction of 'b'. This mechanism is defined as cross-slip in FCC metals. Figure 3-11 shows the schematic representation of the cross-slip mechanism in FCC metals. The screw dislocation at S is free to glide in either of these planes. The non-planar slip surfaces produced by cross-slip is also shown in the figure. Moreover, the event (d) represents the double cross-slip mechanism.

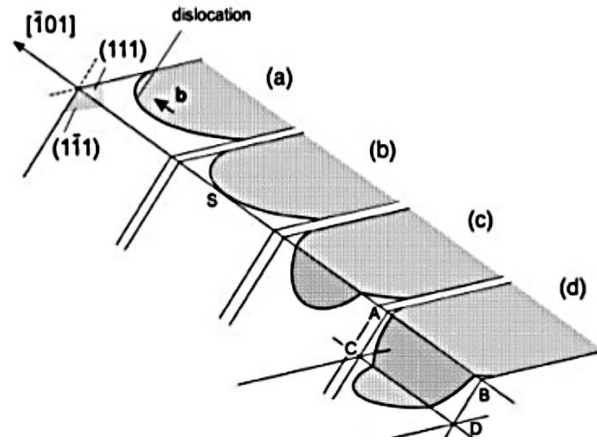


Figure 3-11 The schematic representation of the cross-slip mechanism in FCC metals-The sequence of the events a,b,c,d, respectively [15]

To explain the phenomena related with the storage of dislocations, first the mean-free path of dislocations should be defined. In machining single crystals, the mean free path is limited by the length of the shear zone,  $L$ . Although the shear zone has a size in the range of micrometers, the storage of dislocations is limited by the shear zone due to the rate and the intensity of the shear strain in this plane. By considering this limitation, a physics-based strain hardening expression is developed for the orthogonal cutting process in this study. This consideration also helps to explain the size dependence of material response.

The strain-hardening expression used in this study based on Kocks and Mecking model [17]. This model is analogous to the model of Nix and Gao [30] that is developed to account for the indentation size effect. Finally, GND hardening rate is added to the Kocks-Mecking hardening expression to find the overall strain hardening state.

There are three different terms in the model which consider the strain hardening events, annihilation reactions and the size dependent strain hardening, respectively.

$$\dot{\rho}^a = \left( c_4 \frac{\sqrt{\rho_f^a}}{b} - c_5 (\dot{\gamma}, T) \rho^a + c_6 \frac{1}{bL} \right) |\dot{\gamma}^a| \quad 3.48$$

where the strain hardening term is proportional to the mean forest spacing with constant  $c_4$ , the annihilation term is proportional to the amount of primary dislocations, with the temperature and strain-rate-dependent constant of  $c_5(\dot{\gamma}, T)$  and the last term which considered size dependent strain hardening is proportional with constant  $c_6$ . The size-dependent term of the equation is given as follows:

$$\dot{\rho}_{GND}^{\alpha} = (c_6 \frac{\dot{\gamma}^{\alpha}}{bL}) \quad 3.49$$

It simply assumes that all of the shearing occurs in a very intense shear zone which is characterized by the length scale of  $L$  and  $b$  refers to Burgers vector and  $c_6$  is the scaling constant (values between 0-1) which physically indicates that some portion of the shearing leads to formation of GNDs.

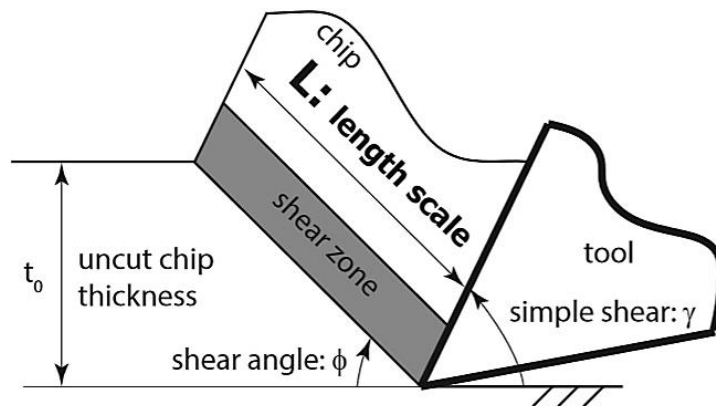


Figure 3-12 : The schematic representation of shear zone and length scale

In this study, it is assumed that due to the part of the shear confined into the shear zone which is specified as the length of the plane,  $L$ , size-dependent dislocations are created. The schematic representation of shear zone and length scale is presented in the figure 3-12 above. The size dependent dislocations are computed by assuming the strain gradients to be proportional to the amount of machining shear,  $\gamma$  and size-dependent dislocations are considered as a fraction of the shear strains. Finally,  $c_6$  constant is used to determine the fraction of the stored dislocations in the shear zone.

### 3.5 Model Constants

Table 4 presents the constants of the dislocation density-based model. The simulations are performed using the same constants for all cutting parameters and crystal orientations. The model constants are used for illustration purposes only.

constant	value	unit	description
b	$2.86 \times 10^{-10}$	m	Burgers vector
K	$1.38 \times 10^{-23}$	J/K	Boltzmann constant
$\Delta F$	$3 \times 10^{-19}$	J	Helmholtz free energy for thermal activation
$\nu_D$	$10^{10}$	1/s	Debye frequency of dislocations
$c_1$	0.5	-	mean-free-path scaling constant for forest dislocation spacing
$c_2$	1	-	geometric constant for the long range flow stress
$c_3$	1	-	adjusting parameter for jump distance
$c_4$	1e-3	-	mean-free-path strain hardening constant
$c_5$	1e-4	-	dislocation annihilation constant
$c_6$	0.5	-	Length-scale constant
$\rho_0$	$10^{13}$	1/m <sup>2</sup>	initial dislocation density

Table 3-2 Description and values of constants used in the dislocation-density-based constitutive laws for single crystal simulations.

In the physics-based models, all parameters have physical meanings as can be seen in the description part of the table 3-2 and their order of magnitude is known [8].  $c_1$  parameter connects the average forest dislocation spacing with the jump distance a mobile dislocation and its range is determined from 1 to 10. For the parameter  $c_2$  is a geometric parameter, which scales the long-range flow stress and usually values between 0.1 and 0.5 are assumed for this parameter.  $c_3$  represents the scaling constant for activation volume or effective obstacle width measured in Burgers vectors and its range assumed from 1 to 10. Parameter  $c_4$  represents the mean-free-path strain hardening constant or the increasing rate for the immobile dislocation densities and the values from  $5.6 \times 10^{-3}$  to  $1.27 \times 10^{-2}$  can be assumed for parameter  $c_4$ . The dislocation annihilation constant,  $c_5$ , or the decreasing term of the immobile dislocation density due to annihilation depended on the both strain rate and temperature and it is assumed in the range of  $10^{-4}$ . The parameter  $c_6$  which accounts of the contribution of the length scale dependent dislocation to the strain hardening behavior of the material, is assumed in the range of 1.

## 4 NUMERICAL SOLUTION PROCEDURE

In this study, the main objective of the algorithm is to find the optimum shear angle value that corresponds to minimum work for a specific crystallographic orientation. As mentioned before, the solution methodology adopted in this study, is suggested by Maniatty et al. [27].

First, the residual,  $\mathbf{Y}$  is defined as a function of the plastic part of the deformation gradient,  $\mathbf{F}^P$  and it is based on the difference between the time-integrated plastic velocity gradient and the plastic velocity gradient (the sum over the slip rates). It is determined by using the Newton-Raphson method iteratively for  $\mathbf{F}^P$ .

$$\mathbf{Y} = \sum_{a=1}^{12} \dot{\gamma}^a \tilde{\mathbf{s}}^a \otimes \tilde{\mathbf{n}}^a - \frac{\mathbf{I} - \mathbf{F}_t^p \mathbf{F}^{p-1}}{\Delta t} \quad 4.1$$

In this method, a fully plastic initial guess is required for the plastic deformation gradient and it is determined from the elastic deformation that is computed from the former deformation increment where the subscript “t” implies the previous time increment, and  $\mathbf{F}_t^e$ , and total deformation gradient at the current time step,  $\mathbf{F}$ .

$${}^0\mathbf{F}^P = \mathbf{F}_t^{e-1} \mathbf{F} \quad 4.2$$

When the plastic part of the deformation gradient is calculated, then  $\mathbf{F}^e$  elastic part of the deformation gradient can be calculated by using the total deformation gradient,  $\mathbf{F}$ . Then by using equation (3.31), Cauchy stress at the deformed configuration can be calculated.

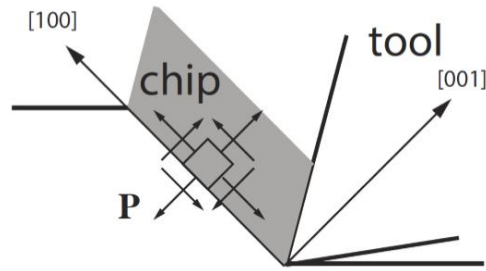


Figure 4-1 The schematic representation of Cauchy Stress State,  $P$ , at the shear reference frame

To calculate the shear force on the shear frame, the multiplication of Cauchy stress with shear plane area is used. Since the Cauchy stress denoted by  $P$  in the fig. (4-1) above, is the stress state at the shear reference frame that is characterized by shear plane normal and shear direction, the stress field has to be projected to the shear plane normal vector  $[001]$  that is also multiplied with sheared area,  $a_s$ , and with the shearing direction  $[100]$  in the sample reference coordinate system.

$$|\mathbf{f}_s| = (\boldsymbol{\sigma}_s : \mathbf{S}) |a_s| \quad 4.3$$

The shear plane area can be calculated by using the equation (4.4) below,

$$a_s = \frac{t_0 w}{\sin \phi} \quad 4.4$$

After determining shear force, and power, shear work can be determined by using the equation (3.13). Finally, for a given cutting orientation and the machining parameters, total power is calculated for every shear angle candidate (with a specific increment) within the allowable range. The shear angle value corresponding to minimum work for a given crystallographic orientation  $\phi$  of the cutting plane normal and cutting direction is selected as the optimal candidate. MATLAB<sup>®</sup> software is used to perform the required numerical calculations and create the resulting plots.

## 5 NUMERICAL RESULTS

In this study, results of the physics-based model obtained by using different machining parameters such as; rake angle,  $\alpha$ , friction coefficient,  $\mu$ , and uncut chip thickness,  $t_0$ . Moreover, the simulations are repeated for the alternate values of the given parameters presented in the table below.

constant	unit	description	nominal value	alternate value
$\alpha$	deg.	rake angle	20	0-40
$\mu$	-	friction coefficient	0,5	0-0,75
V	mm/s	cutting speed	100	10-1000
$t_0$	$\mu\text{m}$	uncut chip thickness	50	5-10
w	mm	width of cut	1	-

Table 5-1 Description and both nominal and alternate values of cutting parameters.

### 5.1 Physics Based Model Results

This chapter consisting of two main parts: in the first part, the effect of crystallographic orientation on the machining response is discussed by using the simulation results of the physics-based model. In the 2<sup>nd</sup> part, the effect of machining parameters on the machining response is investigated. Final part discussed the implementation of the size-effect to the model framework and special size-effect simulations for planning process are presented.

#### 5.1.1 The effect of Crystallographic Orientation on the Cutting Response

In this section, the effect of physical parameters on cutting response is discussed. The material constants in Table 3-2 and the cutting parameters in Table 5-1 are used in the analysis. The aim of this study is to examine the turning response of a single crystal about a defined crystallographic zone axis  $\langle pqr \rangle$ . For orthogonal cutting geometry, crystal orientation is defined with the crystallographic unit vectors along the cutting direction (CD), and cutting plane (CP). Figure 3-3 shows the turning of a crystal with cube orientation.

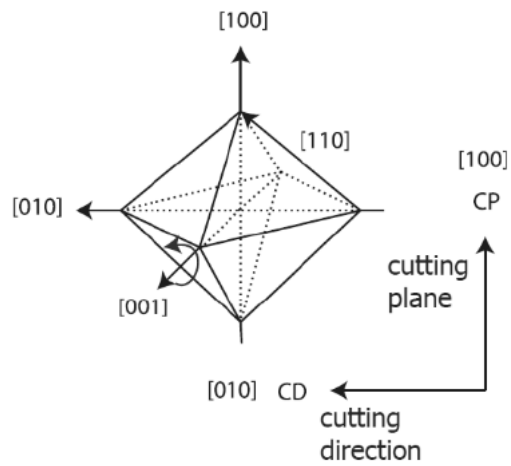


Figure 5-1 Turning of a crystal with cube orientation.  $\langle pqr \rangle$  is the crystallographic direction that the crystal is turned around.  $\langle pqr \rangle$  corresponds to [001] for cube orientation.

Three different zone axes of  $\langle 100 \rangle$ ,  $\langle 110 \rangle$  and  $\langle 111 \rangle$  are used in the simulations. The machining response in the aspect of cutting force and shear angle is presented in Figures 5-1 and 5-2, respectively.

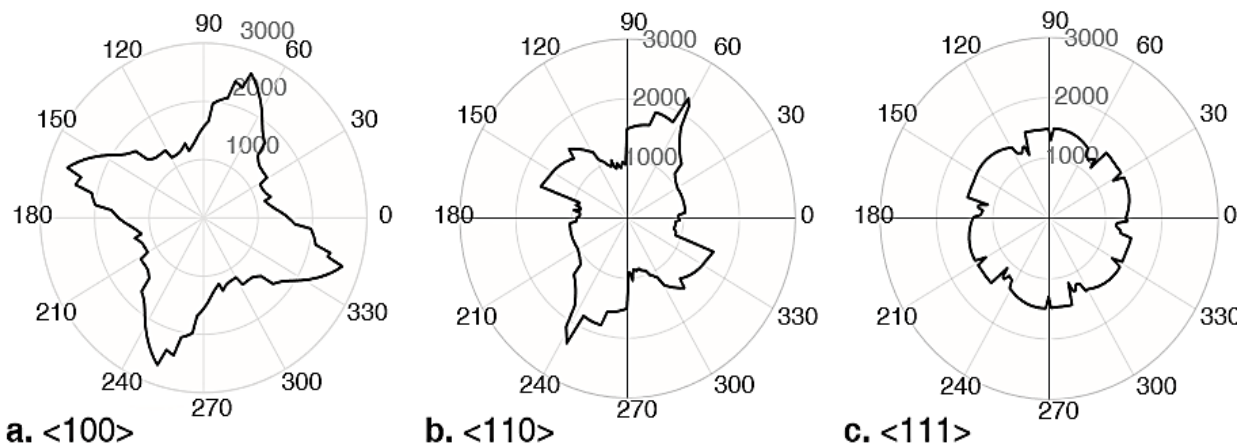


Figure 5-2 Specific cutting energy (MPa) vs. rotation angle  $\theta$  (deg.) about the zone axis  $\{pqr\}$   $\langle 100 \rangle$ ,  $\langle 110 \rangle$  and  $\langle 111 \rangle$ , respectively

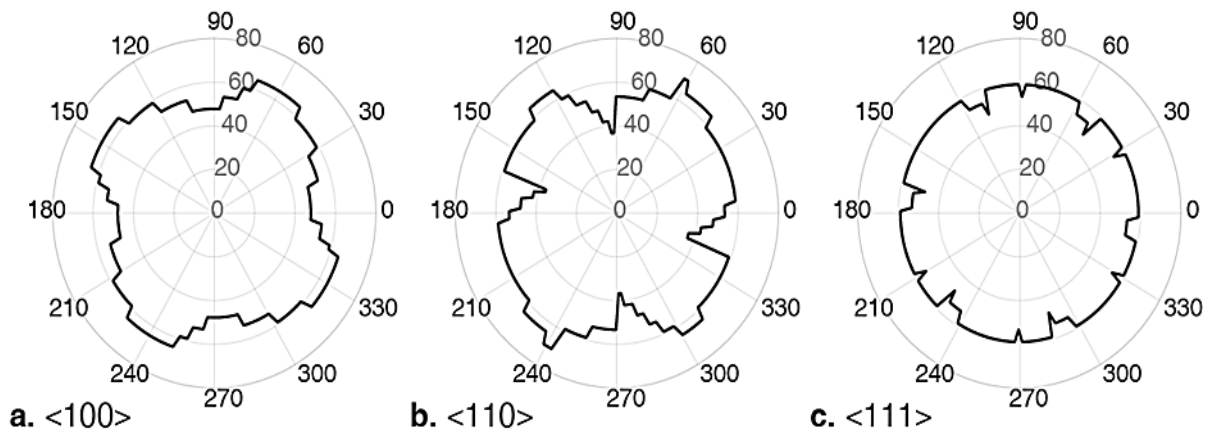


Figure 5-3 Shear angle (deg.) vs. rotation angle  $\theta$  (deg.) about the zone axis  $\{pqr\} \langle 100 \rangle$ ,  $\langle 110 \rangle$  and  $\langle 111 \rangle$ , respectively

As it can be seen in the Figures 5-2 and 5-3, four-fold, two-fold, and six-fold symmetric fluctuations are observed for the crystallographic zone axes of  $\langle 100 \rangle$ ,  $\langle 110 \rangle$ , and  $\langle 111 \rangle$ , respectively, during a single revolution of the workpiece. If only the  $\langle 110 \rangle$  zone axis is considered, it can be said that the two-fold symmetry is observed in cutting force due to the existence of the two peaks. Another important thing is that the smallest average cutting force values are observed when machining about the  $\langle 111 \rangle$  crystallographic axis and the reason for that is the duplex slip due to the in-plane shear. On the other hand, nearly 100% shear strength fluctuation is observed in cutting forces when turning around  $\langle 100 \rangle$  and  $\langle 110 \rangle$  zone axes. As a result, it can be said that cutting forces change significantly along different crystallographic orientations for the micro-machining process of single crystal materials and by using this model, these effects can be captured successfully.

### 5.1.2 The effect of Machining Parameters on the Cutting Response

In this section, the effect of machining parameters such as tool rake angle, uncut chip thickness, friction coefficient between the tool and the workpiece on the cutting response is discussed. Therefore, the cutting simulations are performed for three different rake angle, uncut chip thickness and friction coefficient values.

### 5.1.2.1 The effect of Friction Coefficient

The cutting simulations are performed for three different friction coefficients,  $\mu$ , as 0, 0.5, and 0.75 when turning about  $\langle 100 \rangle$  zone axis. In the figure 5-4, effect of the friction coefficient on the cutting constant during a single revolution of the workpiece.

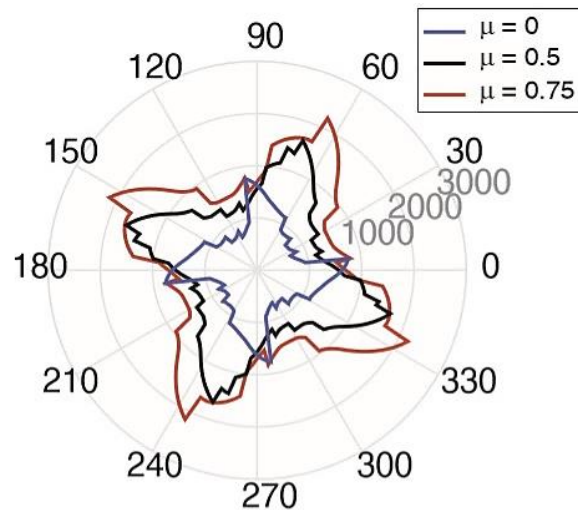


Figure 5-4 Effect of friction coefficient, on the cutting constant (MPa) vs. rotation angle  $\theta$  (deg.) about the zone axis {pqr}

It is clear from the figure 5-4 that, as the friction coefficient increases, the mean value of the corresponding cutting constant increases. Since the friction coefficient is directly related and proportional with friction force, it is expected that cutting force values increase. Moreover, it should be noted that as the friction coefficient decreases, shear angle increases as given by Merchant's minimum work expression, equation (3.1).

### 5.1.2.2 The Effect of Rake Angle

The cutting simulations are performed for three different rake angle values,  $\alpha$ ,  $0^\circ$ ,  $20^\circ$ , and  $40^\circ$ . In the figure 5-5, effect of the friction coefficient on the cutting constant during a single revolution of the workpiece.

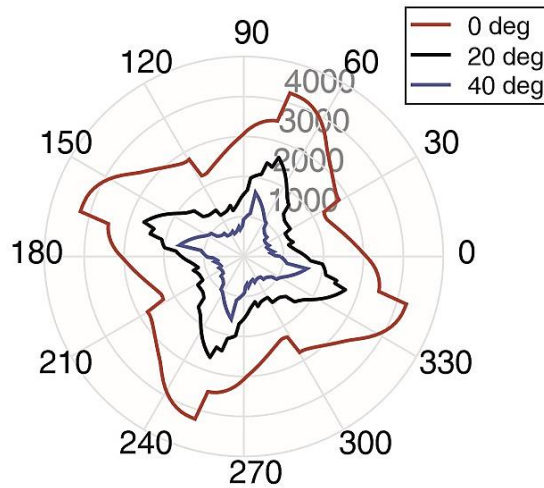


Figure 5-5 Effect of rake angle on the cutting constant (MPa) vs. rotation angle  $\theta$  (deg.) about the zone axis {pqr}

It can be seen from the figure 5-5 that, as the rake angle values decreases, the mean value of the corresponding cutting constant significantly increases. The relation between the rake angle and the cutting force also is already expressed in the Equation (3.10) and it can be said that any increase in the rake angle causes increase in shear angle. One reason for this relation could be the reduction in the contact length between the tool and the chip as rake angle increases which leading to a decrease in the resultant forces and cutting specific energy. Finally, it should be noted that the effect of the rake angle is much greater compared to the all other parameters such as friction coefficient, uncut chip thickness, temperature, etc.

### 5.1.2.3 The effect of Uncut Chip Thickness or Size-Dependence

The cutting simulations are performed for three different uncut chip thickness values,  $t_0$ ,  $5\mu\text{m}$ ,  $10\mu\text{m}$ , and  $50\mu\text{m}$ . In the figure 5-6, effect of the uncut chip thickness on the cutting constant during a single revolution of the workpiece.

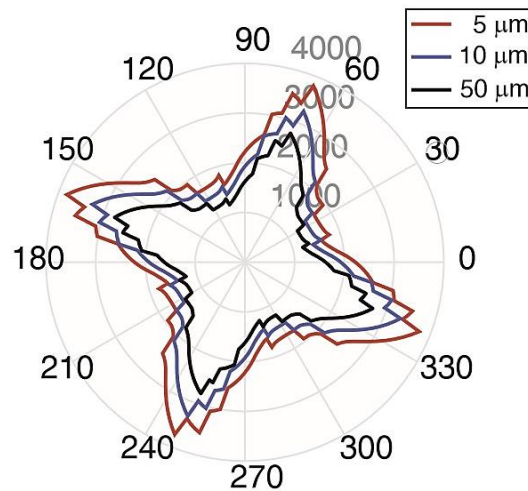


Figure 5-6 Effect of uncut chip thickness values on the cutting constant (MPa) vs. rotation angle  $\theta$  (deg.) about the zone axis {pqr}

It is clear from the figure 5-6 that, as the uncut chip thickness decreases, the increase in the cutting constant values can be observed by using the present model. As expected, when the size values getting smaller strength values of the material increases. The amount of increase in the specific cutting pressure of the material can be considered reasonable if it is compared with the real experimental values. For instance, Oxley and Kopalinsky [18] stated that experimental machining results obtained show that with all other conditions held constant a reduction in uncut chip thickness from 0.2 mm to 0.01 more than doubles the specific cutting pressure.

In order to find the out the initiation of the size effect in the cutting force, experiments are needed to calibrate the model. Size effect depends on the both combination of factors such as work material property, aspect ratio of the chip or shape of the chip etc. Therefore, in this study, the uncut chip thickness value that where the initiation of the size-effect observed is not pointed and no simple rule is presented.

#### 5.1.2.4 The Effect of Temperature

The cutting simulations are performed for three different temperature values, T, 300,400 and 500K. In the figure 5-7, effect of the temperature on the cutting constant during a single revolution of the workpiece.

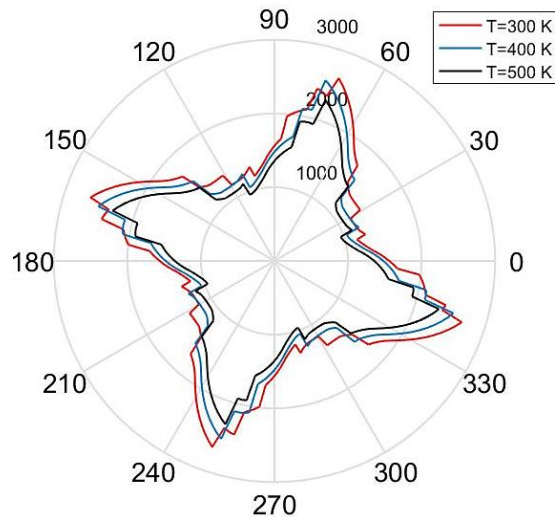


Figure 5-7 Effect of temperature on the cutting constant (MPa) vs. rotation angle  $\theta$  (deg.) about the zone axis of  $\langle 100 \rangle$  direction in rate-sensitive single crystal model

As can be seen in the figure below, if the temperature values increase, the cutting constant values decrease slightly. When the temperature increases, the shear strength of the material decreases ahead the cutting edge due to the thermal softening effect and leading to a decrease in the required cutting forces.

### 5.1.3 Size Dependence Results for Planing Simulations

As mentioned before, although there are many reasons which attributed to the size-effect occurs in machining of single crystals, dependence of shear strength on the uncut chip thickness is considered as the main reason of this phenomena in this study. It is already underlined that an additional strain hardening expression is used in the model in order to incorporate size dependence of shear strength.

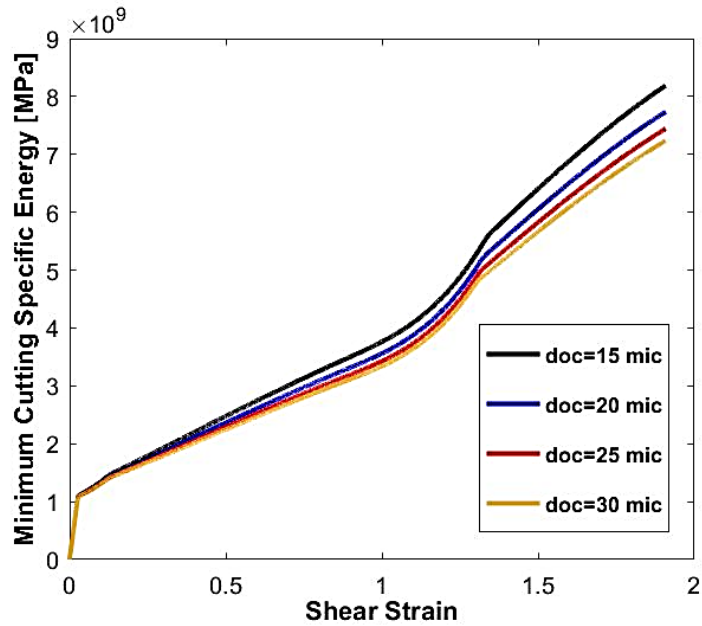


Figure 5-8 Dependence of shear stress on uncut chip thickness values of 15  $\mu\text{m}$ , 20  $\mu\text{m}$ , 25  $\mu\text{m}$  and 30  $\mu\text{m}$ . x axis represents the amount of shear (in radians) along the shear plane.

Figure 5-8 shows the variation of shear stress for different uncut chip thickness values. The uncut chip thickness values of 15  $\mu\text{m}$ , 20  $\mu\text{m}$ , 25  $\mu\text{m}$  and 30  $\mu\text{m}$  are used. The simulations are performed for [100] cutting direction and (010) cutting plane. The size dependence is simulated using only one set of constants that is shown in Table 3-2. To perform calibration for experimental findings, the calibration constant  $c_9$  shall be determined for different uncut chip thickness values.

## 5.2 Taylor Based Model Results

In this section, the results of the rate-insensitive models are represented. This model has as a simpler computational procedure compared to the rate-sensitive crystal plasticity. In order to compare the results obtained by using two models, the rate-insensitive Taylor-based single crystal model for machining is implemented in this work.

In these models, Taylor factor used as a measure to determine the ratio of the crystallographic work to the macroscopic work. By using two different methodology, Taylor factor can be obtained: either by the Taylor work minimization principle, or by the Bishop-Hill work maximization method. The Bishop-Hill method uses 28 possible stress states of a crystal to

estimate the crystallographic work. It is selected in this work owing to its computational simplicity.

The strain increment at the shear reference frame is computed using the deformation gradient defined in Equation (3.14).

$$d\epsilon^{(s)} = \mathbf{F} - \mathbf{I} \quad 5.1$$

The strain is transformed to the crystal reference using the total transformation matrix  $\mathbf{R}$  which is formerly defined in Equation (3.18). The use of the tensor transformation rule applies as expressed in Equation (5.2).

$$d\epsilon^{(c)} = \mathbf{R}d\epsilon^{(s)}\mathbf{R}^T \quad 5.2$$

Then, the amount of work increment can be calculated by considering 28 possible stress states and strain increments,  $\epsilon$  at the crystal reference frame,  $\epsilon^{(c)}$ .

$$dw = -B d\epsilon_{11}^{(c)} + A d\epsilon_{22}^{(c)} + 2F d\epsilon_{23}^{(c)} + 2H d\epsilon_{13}^{(c)} + 2I d\epsilon_{12}^{(c)} \quad 5.3$$

where A,B,F,H and I implies the strain multiplier coefficients and they can be defined as follows:

$$A = \frac{\sigma_{22}^{(c)} - \sigma_{33}^{(c)}}{\sqrt{6\tau_c}}, \quad B = \frac{\sigma_{33}^{(c)} - \sigma_{11}^{(c)}}{\sqrt{6\tau_c}}, \quad F = \frac{\sigma_{23}^{(c)}}{\sqrt{6\tau_c}}, \quad H = \frac{\sigma_{13}^{(c)}}{\sqrt{6\tau_c}}, \quad I = \frac{\sigma_{12}^{(c)}}{\sqrt{6\tau_c}} \quad 5.4$$

To calculate the total work increment, first shear stress should be calculated using the equation below,

$$F_s = \sigma a_s \quad 5.5$$

where  $\sigma$  and  $A_s$  implies the shear stress and shear plane area, respectively.

As one of the major drawback of the rate-insensitive models, the shear stress is obtained as a scalar. Shear stress can be expressed as a multiplication of slip resistance with the Taylor factor, Equation(5.6).

$$\sigma = M \tau_c \quad 5.6$$

where M represents the Taylor Factor. It equals to the ratio of the work increment to the equivalent Von-Mises stress,  $d\epsilon_{eVM}$ , of the strain increment:

$$M = \frac{dW}{d\epsilon_{eVM}} \quad 5.7$$

Critical resolved shear stress can be obtained by using the same relation with passing stress, the long-range stress field which should be exceeded for plastic deformation as already given in the equation 3.38 before. Since an equal amount of slip resistance is assumed for all slip systems; the superscript a is not used in the rate-insensitive crystal plasticity relations.

In this model, the evolution (rate form) of dislocation density is not considered. As a result, total dislocation density can be written in terms of the initial value of the dislocation density and the expected length-scale-dependent dislocation density expression.

$$\rho = \rho_0 + c_6 \frac{\gamma}{bL} \quad 5.8$$

### 5.2.1 The effect of Crystallographic Orientation on the Cutting Response

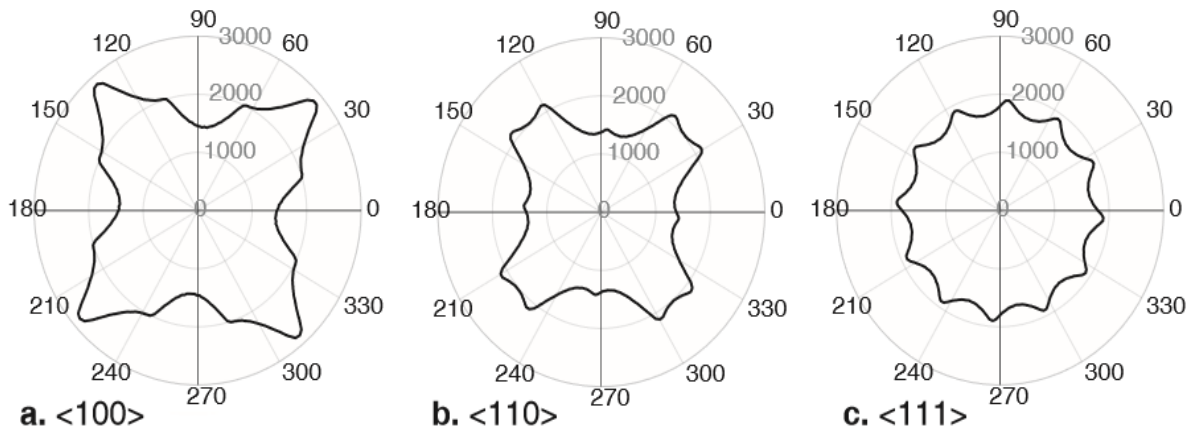


Figure 5-9 Cutting Constant (MPa) vs. rotation angle  $\theta$  (deg.) about the zone axis  $\{pqr\}$   $\langle 100 \rangle$ ,  $\langle 110 \rangle$  and  $\langle 111 \rangle$ , respectively

The variation in cutting constants for three different zone axes are presented in the Figure 5-9. As it can be seen in the figure above, four-fold and six-fold symmetry are observed. As a result, it can be said that the periodicity of the force fluctuations is very similar to that of the rate-sensitive physics-based model. Moreover, that is not the case for the location of maximum forces. Due to the strain hardening effect, the location of the maximum forces is quite different.

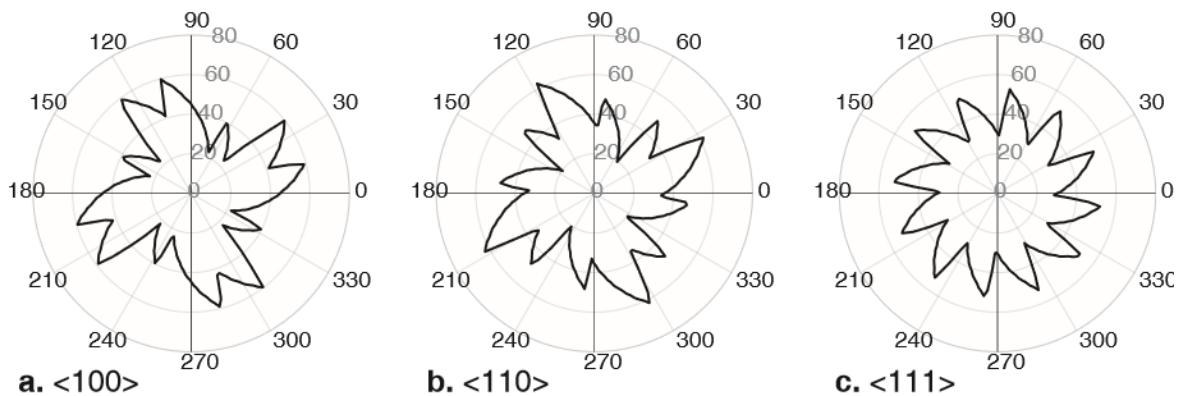


Figure 5-10 Shear angle (deg.) vs. rotation angle  $\theta$  (deg.) about the zone axis  $\{pqr\}$   $\langle 100 \rangle$ ,  $\langle 110 \rangle$  and  $\langle 111 \rangle$ , respectively

The variation in shear angle for three different zone axes are presented in the Figure 5-10. As it can be seen in the figure above, two-fold, four-fold and six-fold symmetry are observed for

the zone axis  $\langle 100 \rangle$ ,  $\langle 110 \rangle$  and  $\langle 111 \rangle$ , respectively. Again, it can be said that the periodicity of the shear angle fluctuations is very similar to that of the rate-sensitive physics-based model.

## 5.2.2 The effect of Machining Parameters on the Cutting Response

In this section, the effect of machining parameters such as tool rake angle, uncut chip thickness, friction coefficient between the tool and the workpiece on the cutting response is discussed for the rate-insensitive models. Therefore, the cutting simulations are performed for three different rake angle, uncut chip thickness and friction coefficient values.

### 5.2.2.1 The effect of Friction Coefficient

The cutting simulations are performed for three different friction coefficients,  $\mu$ , as 0, 0.5, and 0.75 when turning about  $\langle 100 \rangle$  zone axis.

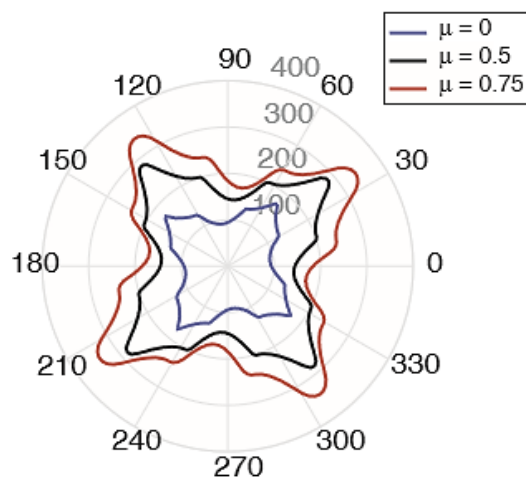


Figure 5-11 Effect of friction coefficient, on the cutting constant (MPa) vs. rotation angle  $\theta$  (deg.) about the zone axis of  $\langle 100 \rangle$  direction in rate-insensitive Taylor-based single crystal model

As it can be seen in the figure 5-11, the effect of friction coefficient can be captured similar cutting force fluctuations as the physics-based rate-sensitive model. However, it is not able to show the fine changes as in the rate-sensitive model.

### 5.2.2.2 The Effect of Rake Angle

The cutting simulations are performed for three different rake angle value,  $\alpha$ , as 0, 20° and 40° when turning about  $\langle 100 \rangle$  zone axis. In the figure 5-11, effect of the rake angle values on the cutting constant during a single revolution of the workpiece.

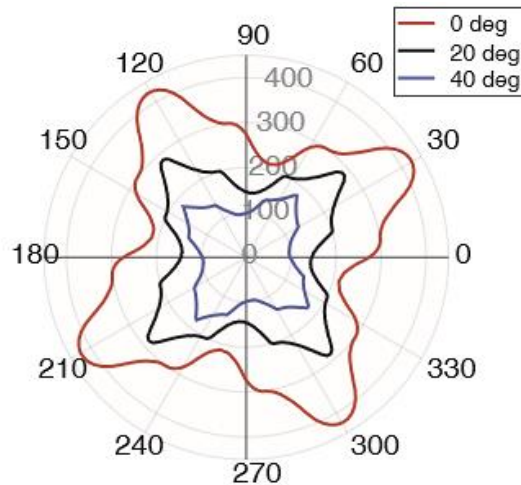


Figure 5-12 Effect of rake angle, on the cutting constant (MPa) vs. rotation angle  $\theta$  (deg.) about the zone axis of  $\langle 100 \rangle$  direction in rate-insensitive Taylor-based single crystal model

As it can be seen in the figure 5-12, the effect of rake angle values can be captured similar cutting force fluctuations as the physics-based rate-sensitive model. However, as the same with the effect of the friction coefficient, it is not able to show the fine changes as in the rate-sensitive model.

### 5.2.2.3 The Effect of Uncut Chip Thickness

The cutting simulations are performed for three different rake angle value,  $t_0$ , 5 $\mu\text{m}$ , 10 $\mu\text{m}$ , and 50 $\mu\text{m}$  when turning about  $\langle 100 \rangle$  zone axis. In the figure 5-13, effect of the uncut chip thickness values on the cutting constant during a single revolution of the workpiece.

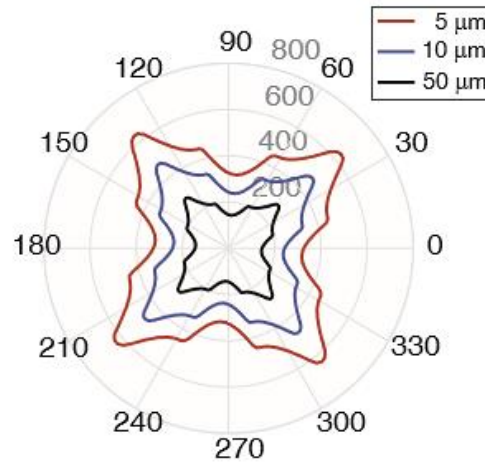


Figure 5-13 Effect of uncut chip thickness, on the cutting constant (MPa) vs. rotation angle  $\theta$  (deg.) about the zone axis of  $\langle 100 \rangle$  direction in rate-insensitive Taylor-based single crystal model

As it can be seen in the figure 5-13, the effect of uncut chip thickness values can be captured similar cutting force fluctuations as the physics-based rate-sensitive model. However, as the same with the other machining parameters investigated, it is not able to show the fine changes as in the rate-sensitive model.

### 5.3 Experimental Validation

In this section, experimental validation of the physics-based model and the Taylor-based rate-insensitive model is discussed. Experimental validation is done by using the data sets in the work of Cohen. In other words, the calibration of the proposed model is achieved by determining the material constants ( $c_1$ - $c_6$ ) and the initial dislocation density by trial and error. The calibration of the Taylor-based model is much simpler and quicker compared to physics-based model. Machining parameters used in the experiments are presented in the table below.

test- id	material	$\alpha(^{\circ})$	w(mm)	V(mm/s)	$t_0$ (mm)	T( $^{\circ}$ K)
test- 3	Al	40	1.500	0.55	0.1143	300
test- 8	Al	50	1.500	0.55	0.1144	300
test- 13	Cu	20	2.100	0.55	0.1145	300
test- 15	Cu	40	2.100	0.55	0.1146	300

Table 5-2 The machining parameters used in the experiments of Cohen[6]

Only uncertainty in the values of the parameters is the width of cut value. Since the exact values were not presented in the thesis, the same values are assumed for the uncut chip thickness for the same material type to make it more consistent. The amount of friction is considered as constant between the tool rake face and chip and the value of the friction angle used as 50 deg.

test- id	$C_{11}$ (Gpa)	$C_{12}$ (Gpa)	$C_{44}$ (Gpa)	(Taylor-based) $\rho_0$ (1/m <sup>2</sup> )	(Physics-based) $\rho_0$ (1/m <sup>2</sup> )	$c_1$	$c_2$	$c_3$	$c_4$	$c_5$	$c_6$
test- 3	112.6	66.3	55.6	$3.5 \times 10^{14}$	$1 \times 10^{12}$	1	0.1	1	$1 \times 10^{-4}$	$1 \times 10^{-5}$	0.5
test- 8	112.6	66.3	55.6	$3.5 \times 10^{14}$	$1 \times 10^{12}$	1	0.1	1	$1 \times 10^{-4}$	$1 \times 10^{-5}$	0.5
test- 13	168	121.4	75.4	$7 \times 10^{15}$	$6 \times 10^{12}$	1	0.4	1	$5 \times 10^{-4}$	$5 \times 10^{-5}$	0.5
test- 15	168	121.4	75.4	$7 \times 10^{15}$	$2 \times 10^{13}$	1	0.4	1	$5 \times 10^{-4}$	$5 \times 10^{-5}$	0.5

Table 5-3 Material constants used as model constants for experimental data of Cohen

The material constants obtained after the numerical fitting are presented in the table 5-3 above. Since the material constants  $c_1$ - $c_6$  depend on the material type, the same values are used independent of the material. The values of the initial dislocation density could be different for the same material; due to the fact that, initial dislocation density of the material depends on the number of machining passes and clean-up passes which could affect the sub-surface damage.

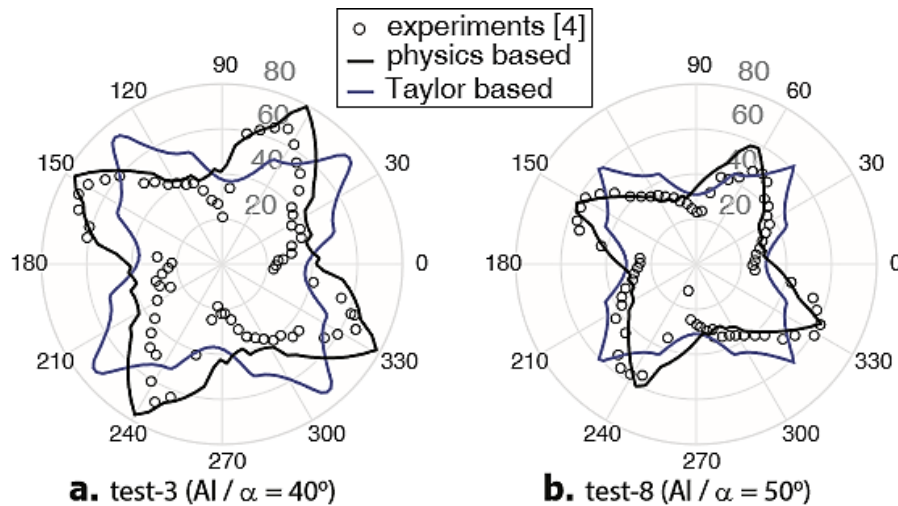


Figure 5-14 The variation of the Cutting force for turning a single crystal Aluminum about crystallographic zone axis of  $\langle 100 \rangle$  direction for test-3 (Al- $\alpha=40$  deg) and test-8 (Al-  $\alpha=50$  deg), respectively.

As can be seen in the figure 5-14 above, the physics-based model can capture the variations in the cutting force. In the aspect of periodicity, Taylor-based model can also be considered as successful. However, the location of the peak forces and force signatures are not predicted accurately.

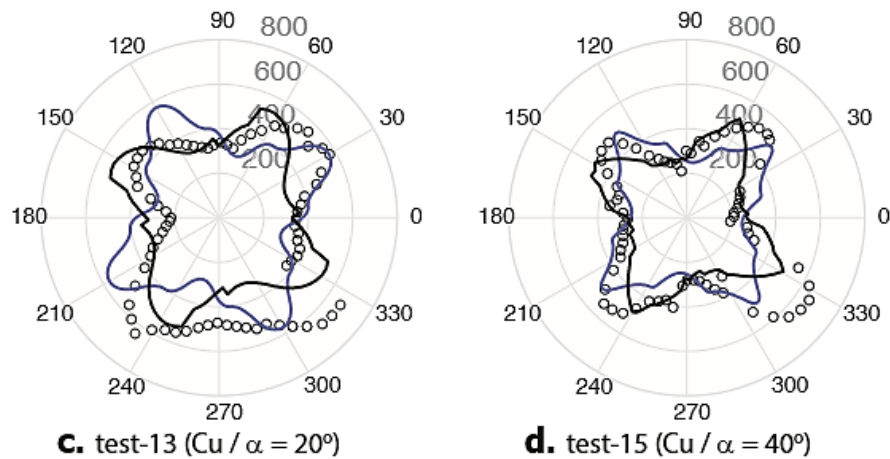


Figure 5-15 The variation of the Cutting force for turning a single crystal Copper about crystallographic zone axis of  $\langle 100 \rangle$  direction for test-13 (Cu- $\alpha$ =20 deg) and test-15 (Cu- $\alpha$ =40 deg), respectively.

Figure 5-15 shows the variation of the cutting force for turning a single crystal copper about crystallographic zone axis of  $\langle 100 \rangle$  direction for test-13 and test-15. In analogy to the validation of the Aluminum cutting results, the physics-based model can capture the variations in the cutting force better than the rate-insensitive model. It is expected, due to the volume constancy assumption in Taylor-models which is a wrong assumption when large shears involved during the process. On the other hand, by using the physics-based model stress on the shear plane can be obtained in its full tensorial form.

In the second part of the validation, comparisons between the measured shear angle values from the work of Cohen [6] and simulation results presented. As can be seen in the figure 5-16 and 5-17, four-fold symmetry is observed for the case of shear angle variation during cutting Al sing crystals. The physics-based model can predict the periodicity in the shear angle values. The only difference observed is for the range of shear angle values. The experimental shear angle values are much smaller compared to the physics-based model's predictions.

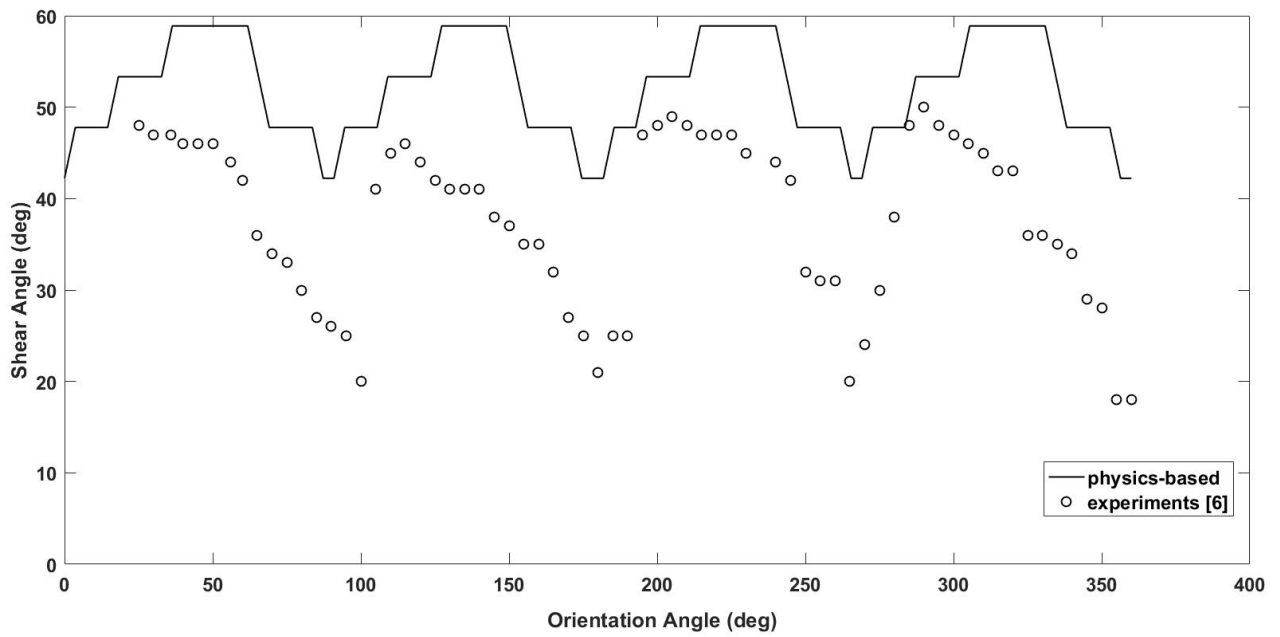


Figure 5-16 The variation of the Shear Angle values for turning a single crystal Aluminum about crystallographic zone axis of  $\langle 100 \rangle$  direction for test-3 ( $\text{Al-}\alpha=40$  deg)

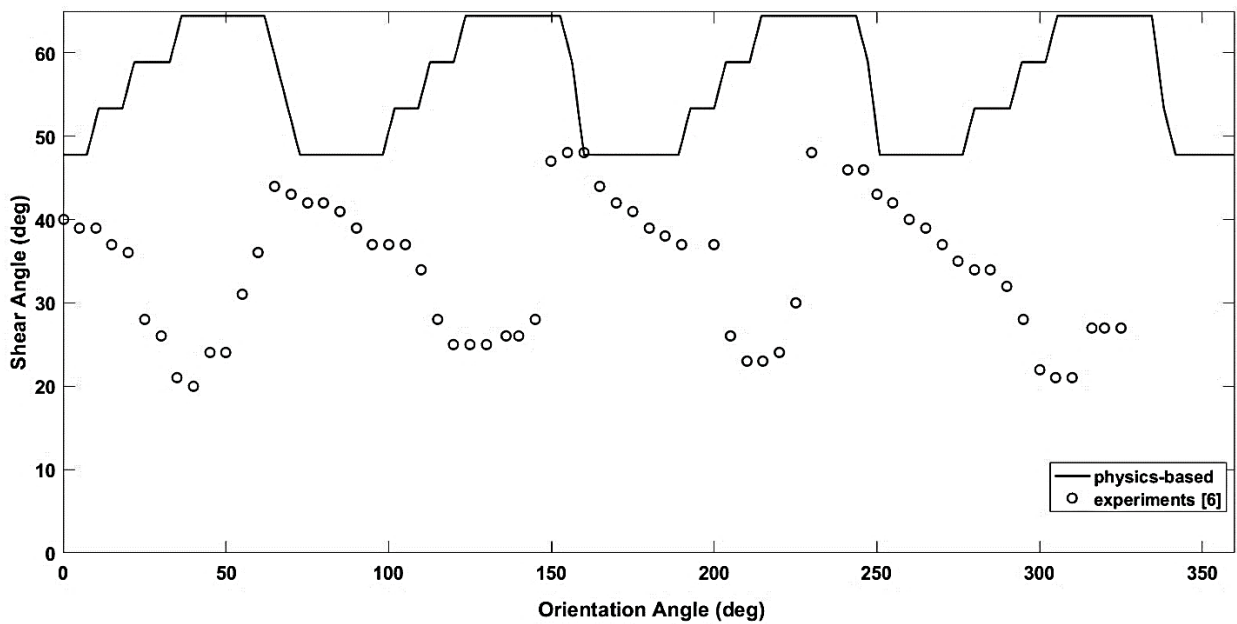


Figure 5-17 The variation of the Shear Angle values for turning a single crystal Aluminum about crystallographic zone axis of  $\langle 100 \rangle$  direction for test-8 ( $\text{Al-}\alpha=50$  deg)

As the same with the case in cutting of Al single crystals, the four-fold symmetry is observed for the case of shear angle variation during cutting Cu single crystals. The physics-based model

can predict the periodicity in the shear angle values as presented in the figure 5-18 and 5-19. Again, the only difference observed is for the range of shear angle values. The experimental shear angle values are much smaller compared to the physics-based model's predictions.

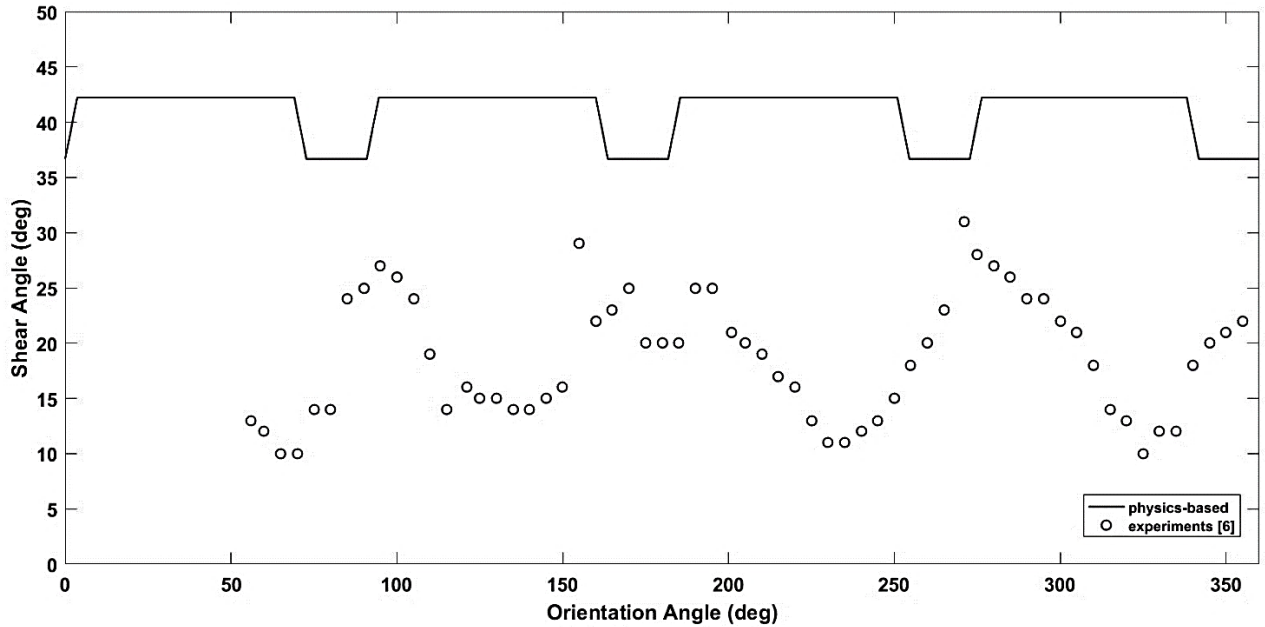


Figure 5-18 The variation of the Shear Angle values for turning a single crystal Copper about crystallographic zone axis of  $\langle 100 \rangle$  direction for test-13 ( $\text{Cu-}\alpha=20$  deg)

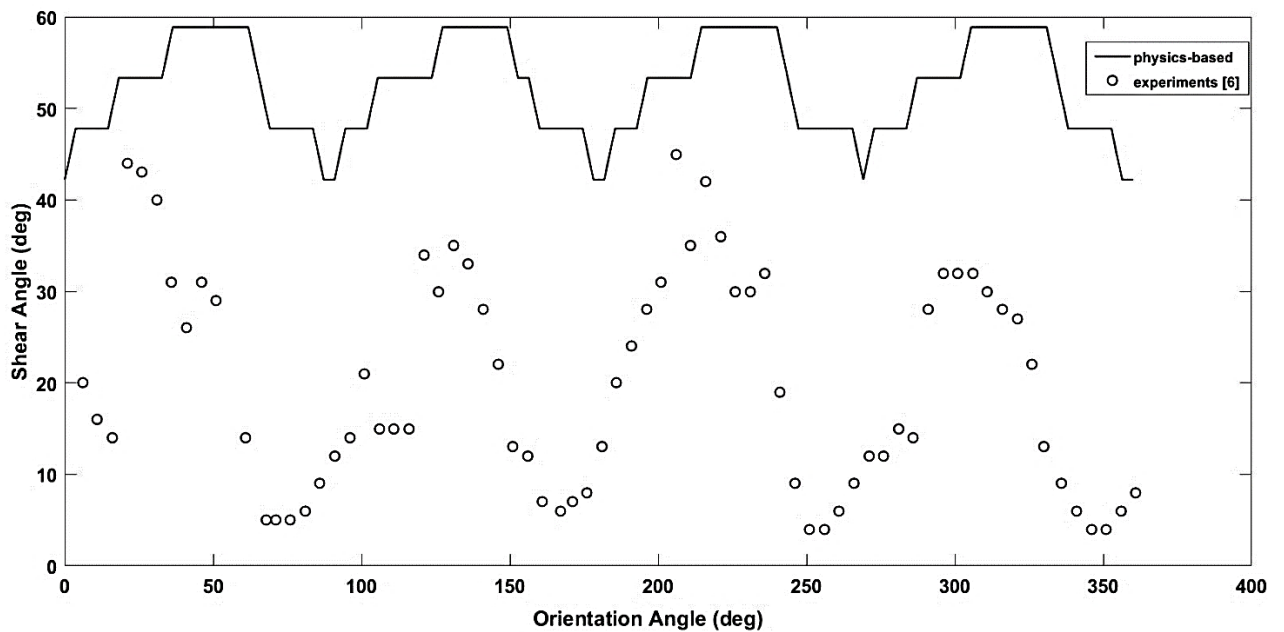


Figure 5-19 The variation of the Shear Angle values for turning a single crystal Copper about crystallographic zone axis of  $\langle 100 \rangle$  direction for test-15 ( $\text{Cu-}\alpha=40$  deg)

The potential reasons for the difference between the experimental results and the simulation results of the physics-based model can be listed as follows:

- In this study, since the effect of edge radius of the tool is ignored and only shear type of deformation is considered in the models, all mechanisms related with edge radius such as ploughing are also neglected.
- As mentioned before, changes in the friction coefficient with crystallographic orientation is also neglected. However, the experimental study that model is calibrated with shows that highest friction coefficient was measured for the  $\langle 1\ 0\ 0 \rangle$  cutting direction.
- Similar with friction angle, the variation in the rake angle during the experiments with the effects of edge radius and built-up-edge is also neglected in the model.
- Finally, inaccuracies in the experimental setup of the micro-machining process are also neglected.

## 6 CONCLUSIONS & FUTURE WORKS

### 6.1 Conclusions

Last but not the least, this thesis presented a physics-based crystal plasticity model which is developed for micro-machining and implemented for the turning of single crystals. Due to the complex nature of the deformation processes in real-life, the need for comprehensive modelling frameworks distinguish. However, long computational times and high cost values associated with these tools load the dice against finite element models. On the other hand, the proposed model provides a simpler way compared to finite element models to understand the basic mechanism of the deformation during turning of single crystals.

The physics-based model can capture the effect of the machining parameters such as rake angle, friction coefficient, uncut chip thickness, cutting speed, temperature etc., on the cutting force and shear angle. Furthermore, it can predict the cutting force fluctuations which occurs due to the crystallographic orientation, accurately. In addition, size dependence of shear strength is introduced by the shear strain getting confined to a smaller region as the depth of cut decreases in a crystal plasticity framework. Shear plane length is assumed as a limit for the mean-free-path of the dislocations in the shear plane. The corresponding increase in the strength is computed by the strain hardening effect of these additional statistically stored dislocations. As a result, the size dependence of cutting is incorporated to the model in a physically-based consistent manner and it is capable to model dependence of shear stress on the uncut chip thickness.

The proposed model reveals temperature and strain-rate dependence of the material response once the calibration of the model constants is performed. If phenomenological models were used, i.e. Johnson-Cook model, the model calibration including all of the model constants has to be performed at every different temperature. On the other hand, the present model takes account of the temperature dependence by considering a single constant to be calibrated (dislocation annihilation constant  $c_5$ ).

The proposed crystal plasticity model reveals a better correlation. Taylor-based models cannot be used for capturing fine changes in the machining response. Only the general features of the

machining response e.g. periodicity of the force fluctuations with the changes in the crystallographic orientation can be captured by using these models. Another restriction is the volume constancy assumption used in the Taylor-based models which is not applicable to problems involving high amounts of shear strains. In addition, strain rate and temperature dependence are not included to the Taylor based rate-insensitive models. The advantages of Taylor-based models are; i. computationally efficiency, and ii. simplicity compared to the physics-based models.

To show the model deliverables, experimental validation of the model is presented in the last chapter of the thesis. According to the results, it can be said that the model reveals a better fit to the experimental cutting force patterns than the rate-insensitive Taylor based models. Therefore, the experimental changes in the cutting forces of single crystals of Cohen [6] was captured successfully by using the proper material constants ( $c_1$ - $c_6$ ) and the initial dislocation density values.

## **6.2 Suggestions for the Future Work**

Suggestions for future work include the extension of the model for other machining processes such as turning, facing, milling, and drilling by transforming the orthogonal model to the oblique cutting geometry. In this study, sharp tool assumption is considered but the effect of tool edge radius can also be modelled by taking account of the change in the rake angle. In this case, total work can be considered in two separate parts; in one part where the work does not change with the tool edge radius since it does not affect the shear angle value and in the second part, the effect of tool edge radius is modelled by taking account of the change in the rake angle leading to a change in the total work.

Last but not the least, this study focused on the materials with FCC crystal structure, due to the its wide-spread use in electronics (i.e. Copper) and aerospace industry (i.e. Aluminum alloys and Nickel-based superalloys) and the material anisotropy observed during micro machining of these materials. However, this study can be extended to other materials with different crystal structures by making modifications with respect to the physics of relevant plastic deformation mechanisms. In addition, from this single crystal model, the macroscopic response of the polycrystal could also be derived and this also can be considered as a future work for this study.

## 7 REFERENCES

- [1] Altintas, Y. (2000). *Manufacturing Automation – Metal Cutting Mechanics, Machine Tool Vibrations and CNC Design*. Cambridge University Press.
- [2] Austin, R., & McDowell, D. (2010). A dislocation-based constitutive model for viscoplastic deformation of FCC metals at very high strain rate. *International Journal of Plasticity*, 1-24.
- [3] Backer, W. R., Marshall, E., & Shaw, M. (1952). *Transactions of ASME*.
- [4] Blackley, W., & Scattergood, R. (1991). Ductile-regime machining model for diamond turning of brittle materials . *International Journal of Precision Engineering* , 95-103.
- [5] Callister, W. (2001). *Fundamentals of Materials Science and Engineering*. New York: J. Wiley & Sons.
- [6] Cohen, P. (1982). *The Orthogonal In-Situ Machining Of Single and Polycrystalline Aluminum and Copper*. The Ohio State University. The Ohio State University.
- [7] Conrad, H. (1970). *Material Science and Engineering* , 265-273.
- [8] Demir, E. (2016). A physically based constitutive model for FCC single crystals with a single state variable per slip system. *Modelling and Simulation in Materials Science and Engineering* .
- [9] Demir, E., Roters, F., & Raabe, D. (2010). Bending of single crystal micro cantilever beams of cube orientation: Finite element model and experiments. *Jour. Mech. Phys. Solids*, 1599-1612.
- [10] Demiral, M., Roy, A., El Sayed, T., & Silberschmidt, V. V. (2014). Numerical modelling of micro-machining of f.c.c. single crystal: Influence of strain gradients. *Computational Materials Science*, 273-278.
- [11] Fang, N. (2002). Slip-line modeling of machining with a rounded-edge tool—Part I: new model and theory . *Journal of the Mechanics and Physics of Solids* , 715-742.
- [12] Franciosi, P., & Zaoui, A. (1982). Multislip in FCC crystals, a theoretical approach compared with experimental data. *Acta Metall*, 1627-1637.

- [13] Gao, H., & Huang, Y. (2002). Geometrically necessary dislocation and size-dependent plasticity. *Scripta Materialia*, 113-118.
- [14] Hansen, B., Beyerlein, I., Bronkhorst, C., Cerreta, E., & Dennis-Koller, D. (2013). A dislocation-based multi-rate single crystal plasticity model. *International Journal of Plasticity*, 129-146.
- [15] Hull, D., & Bacon, D. (2001). *Introduction to Dislocations*. Butterworth-Heinemann (B/H) press.
- [16] Joshi, S., & Melkote, S. (2004). An explanation for the Size-Effect in Machining Using Strain Gradient Plasticity. *Journal of Manufacturing Science and Engineering*, 679-684.
- [17] Kocks, U., & Mecking, H. (2003). Physics and phenomenology of strain hardening: the FCC case. *Progress in Materials Science*, 171-273.
- [18] Kopalinsky, E., & Oxley, P. (1984). Size effects in metal removal processes. *Institute of Physics Conference Series*, 389-396.
- [19] Kota, N., & Ozdoganlar, O. (2010). A Model-Based Analysis Of Orthogonal Cutting For Single-Crystal FCC Metals Including Crystallographic Anisotropy. *Machining Science and Technology: An International Journal*, 102-127.
- [20] Kota, N., Rollet, A. D., & Ozdoganlar, B. O. (2011). A Rate-Sensitive Plasticity-Based Model for Machining of Face-Centered Cubic Single-Crystals—Part I: Model Development. *Journal of Manufacturing Science and Engineering*.
- [21] Kuhlmann-Wilsdorf, D. (1987). Energy minimization of dislocations in low-energy dislocation structures. *Physica status solidi sol. (a)* 104, 121-144.
- [22] Larsen-Basse, J., & Oxley, P. (1973). Effect of strain rate sensitivity on scale phenomena in chip formation. *Proceedings of the 13th International Machine Tool Design & Research Conference*, , 209-216.
- [23] Lee, E. (1969). Elastic-plastic deformation at finite strains. *Series E, Journal of Applied Mechanics Transactions of the ASME*. , 1-6.

- [24] Lee, W., & Zhou, M. (1993). A theoretical analysis of the effect of crystallographic orientation on chip formation in micromachining. *International Journal of Machine Tools and Manufacture* , 439-447.
- [25] Lee, W., Cheung, C., & To, S. (2002). A Microplasticity Analysis of Micro-Cutting Force Variation in Ultra-Precision Diamond Turning. *Transactions of the ASME*, 170-177.
- [26] Liu, K., & Melkote, S. N. (2006). Finite element analysis of the influence of tool edge radius on size effect in orthogonal micro-cutting process. *International Journal of Mechanical Sciences*, 650-660.
- [27] Maniatty, A., Dawson, P., & Lee, Y. (1992). .A Time Integration Algorithm for Elastoviscoplastic Cubic-Crystals Applied to Modeling Polycrystalline Deformation. *Int. Jour. for Num. Met. in Eng*, 1565-1588.
- [28] Mian, A., Driver, N., & Mativenga, P. (2011). Identification of factors that dominate size effect in micro-machining. *International Journal of Machine Tools & Manufacture*, 383-394.
- [29] Moriwaki, T., Okuda, K., & Shen, J. G. (1993). Study of Ultraprecision Orthogonal Microdiamond Cutting of Single-Crystal Copper. *JSME International Journal*, 400-406.
- [30] Nix, W., & Gao, H. J. (1998). Indentation size effects in crystalline materials: A law for strain gradient plasticity. *Journal of the Mechanics and Physics of Solids*.
- [31] Passchier, C. W., & Trouw, R. A. (2005). *Microtectonics*. Springer-Verlag Berlin Heidelberg.
- [32] Raabe, D., Klose, P., Engl, B., Imlau, K.-P., Friedel, F., & Roterz, F. (2002). Concepts for Integrating Plastic Anisotropy into Metal Forming Simulations. *Advanced Engineering Materials*, 169-180.
- [33] Sato, M. Y., & Takabayashi, T. (1991). A Study on the Microcutting of Aluminum Single Crystals. *JSME International Journal*, 540-545.
- [34] Shahba, A., & Ghosh. (2016). Crystal plasticity FE modeling of Ti alloys for a range of strain-rates. Part I: A unified constitutive model and flow rule. *International Journal of Plasticity*, 48-68.

- [35] To, S., Lee, W. B., & Chan, C. Y. (1997). Ultraprecision Diamond Turning of Aluminum Single Crystals. *Journal of Materials Processing Technology*, 157-162.
- [36] Ueda, K., & Iwata, K. (1980). Chip Formation Mechanism in Single Crystal Cutting of  $\beta$ -Brass . *CIRP Annals-Manufacturing Technology*, 41-46.
- [37] Zahedi, A. S., Roy, A., & Silberschmidt, V. V. (2014). Variation of cutting forces in machining of f.c.c. single crystals. *Acta Mechanica* .
- [38] Zhou, M., & Ngoi, B. (2001). Effect of tool and workpiece anisotropy on microcutting processes. *Proceedings of the Institution of Mechanical Engineers*, 13-19.

## 7.1 Appendix A: Algorithm Flowchart

